ACS NANO
Cite This: ACS Nano 2018, 12, 12401−12415
www.acsnano.org

ARTICLE

Sequentially Triggered Delivery System of Black Phosphorus Quantum Dots with Surface Charge-Switching Ability for Precise Tumor Radiosensitization

Leung Chan,[†] Pan Gao,[†] Wenhua Zhou,[‡] Chaoming Mei,[†] Yanyu Huang,[†] Xue-Feng Yu,*[,‡] Paul K. Chu,[§] and Tianfeng Chen*[,†]

[†]Department of Chemistry, Jinan University, Guangzhou, 510632, People's Republic of China

[‡]Center for Biomedical Materials and Interfaces, Shenzhen Institutes of Advanced Technology, Chinese Academy of Sciences, Shenzhen, 518055, People's Republic of China

[§]Department of Physics and Department of Materials Science and Engineering, City University of Hong Kong, Tat Chee Avenue, Kowloon, Hong Kong, China

S *Supporting Information*

ABSTRACT: **Cancer radiotherapy suffers from drawbacks such as radiation resistance of hypoxic cells, excessive radiation that causes damage of adjacent healthy tissues, and concomitant side effects. Hence, radiotherapy sensitizers with improved radiotherapeutic performance and requiring a relatively small radiation dose are highly desirable. In this study, a nanosystem based on poly(lactic-*co*-glycolic acid) (PLGA) and ultrasmall black phosphorus quantum dots (BPQDs) is designed and prepared to accomplish precise tumor radiosensitization. The PLGA nanoparticles act as carriers to package the BPQDs to avoid off-target release and rapid degradation during blood circulation. The nanosystem that targets the polypeptide peptide motif Arg-Gly-Asp-Gys actively accumulates in tumor tissues. The 2,3-dimethylmaleic anhydride shell decomposes in an acidic microenvironment, and the nanoparticles become positively charged, thereby favoring cellular uptake. Furthermore, glutathione (GSH) deoxidizes the disulfide bond of cystamine and sequentially triggers release of BPQDs, rendering tumor cells sensitive to radiotherapy. The treatment utilizing the PLGA$_{-SS-}$D@BPQDs nanosystem and X-ray induces cell apoptosis triggered by overproduction of reactive oxygen species. In the *in vivo* study, the nanosystem shows excellent radiotherapy sensitization efficiency but negligible histological damage of the major organs. This study provides insights into the design and fabrication of surface-charge-switching and pH-responsive nanosystems as potent radiosensitizers to achieve excellent radiotherapy sensitization efficacy and negligible toxic side effects.**

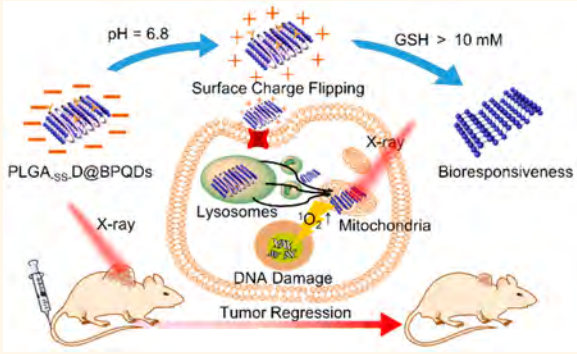

KEYWORDS: *radiosensitization, black phosphorus, stability, surface charge-switching ability, bioresponsive property*

Radiotherapy, one of the three major cancer therapeutic methods, depends on the use of high-energy X-rays or γ-rays to trigger tumor ablation *via* radiation-induced DNA damage and cell apoptosis.[1−3] The radiation also activates water molecules to produce reactive oxygen species including ·OH, ·H, H_2O^+, H_3O^+, and $\cdot O_2^-$ which activate the MAPKs and p53 pathways to induce cell apoptosis. Although radiotherapy is very common in cancer treatment, it has drawbacks such as variation of radiosensitivity among individuals, undesirable side effects, and radiation resistance, and therefore, more efficient radiotherapy sensitizers are desirable. Recently, nanoscale sensitizers have been investigated,[4] for instance, precious metal nanomaterials,[5,6] third-row transition elements,[7−11] ferrite-based nanomaterials,[12−14] and semiconductor nanomaterials.[15,16] The first two with obvious X-ray mass attenuation coefficients improve accumulation of radiative energy in cancer cells to generate scattered photons, photoelectrons, and Auger electrons.[17] These secondary electrons have narrow effects and damage cancer

Received: August 25, 2018
Accepted: November 8, 2018
Published: November 8, 2018

DOI: 10.1021/acsnano.8b06483
ACS Nano 2018, 12, 12401−12415

Scheme 1. Rational design and application of PLGA$_{-SS-}$D@BPQDs to tumor radiotherapy.

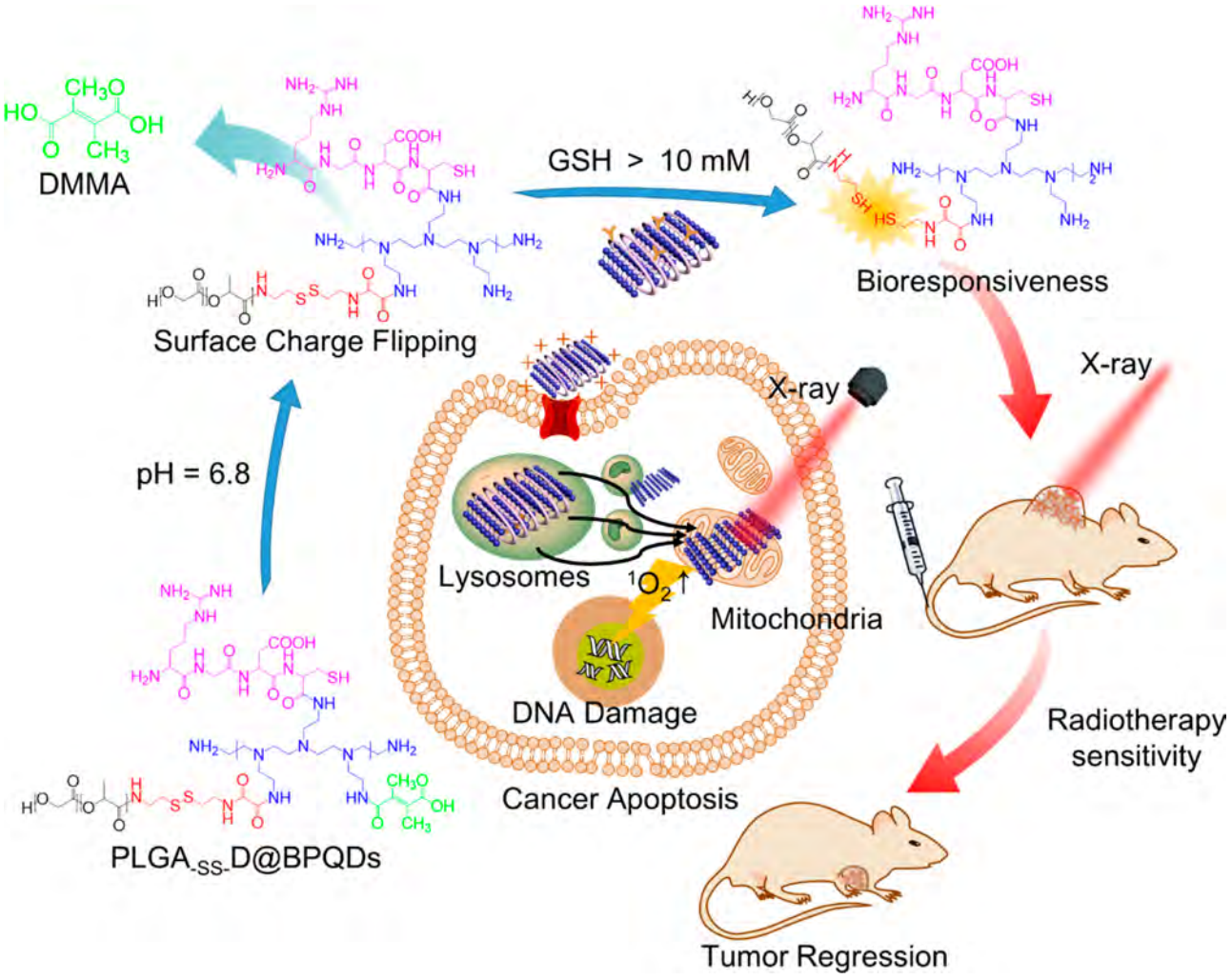

tissues around the nanomaterials except normal tissues. Superparamagnetic iron oxide particles (SPIONs) are ferrite-based nanomaterials and can be used in not only magnetic resonance imaging (MRI) but also cancer radiotherapy.[18] After X-ray irradiation, SPIONs catalyze water molecules to produce reactive oxygen species (ROS) by Fenton's reaction and Haber–Weiss reaction.[19−21] Unfortunately, few of them are suitable for *in vivo* cancer radiotherapy. The ideal radiotherapeutic nanoagent should have high radiosensitization, a suitable size, and proper surface functionalization for specific tumor targeting as well as biocompatibility and biodegradability to minimize toxicity to normal tissues. Therefore, it is highly desirable to develop a sensitizer for clinical radiotherapy.

As a type of two-dimensional (2D) materials with good biocompatibility,[22] black phosphorus (BP) has aroused increasing interest in the biomedical areas due to its excellent properties. BP nanosheets and BP quantum dots (BPQDs), which exhibit broad light absorption, high photothermal conversion efficiency, and high singlet oxygen generation efficiency, have been adopted as agents in photothermal therapy (PTT) and photodynamic therapy (PDT) for cancer.[23,24] Furthermore, owing to the puckered honeycomb 2D structure with atomic thickness and large surface-to-volume ratios, BP nanomaterials have recently been used in delivery of drugs[25] and bioactive macromolecules.[26] Compared with other inorganic nanomaterials, BP is especially attractive due to its biodegradability. Nonetheless, although it is converted into nontoxic phosphite/phosphate ions under physiological conditions, natural degradation may not be preferred in some situations. For example, it is indeed beneficial in drug metabolism and excretion to eliminate potential cytotoxicity caused by long-term exposure of BP *in vivo*, but on the other hand, the intrinsic instability under physiological conditions may limit in-depth research and some clinical applications.[27]

In this study, BPQDs are adopted as radiosensitizing drugs and a nanosystem based on poly(lactic-*co*-glycolic acid) (PLGA) (PLGA$_{-SS-}$D@BPQDs) is designed and fabricated for precise tumor radiosensitization. PLGA is approved clinically by the Food and Drug Administration (FDA) because of its low toxicity and excellent biocompatibility.[28,29] In this nanosystem, cystamine with disulfide linkage serves as the bioresponsive trigger that can be broken by the reductive glutathione (GSH) rich in the tumor microenvironment.[30] Polyethylenimine (PEI) is connected to cystamine with an equal molecular weight of oxalic acid,[31] and this cationic polymer with abundant amino groups is used to improve the hydrophilicity and cellular uptake of the nanosystem and to provide sites for further chemical modification.[32,33] Conjugation of 2,3-dimethylmaleic anhydride (DMMA) onto the surface of the nanosystem produces a pH-responsive shell to

DOI: 10.1021/acsnano.8b06483
ACS Nano 2018, 12, 12401−12415

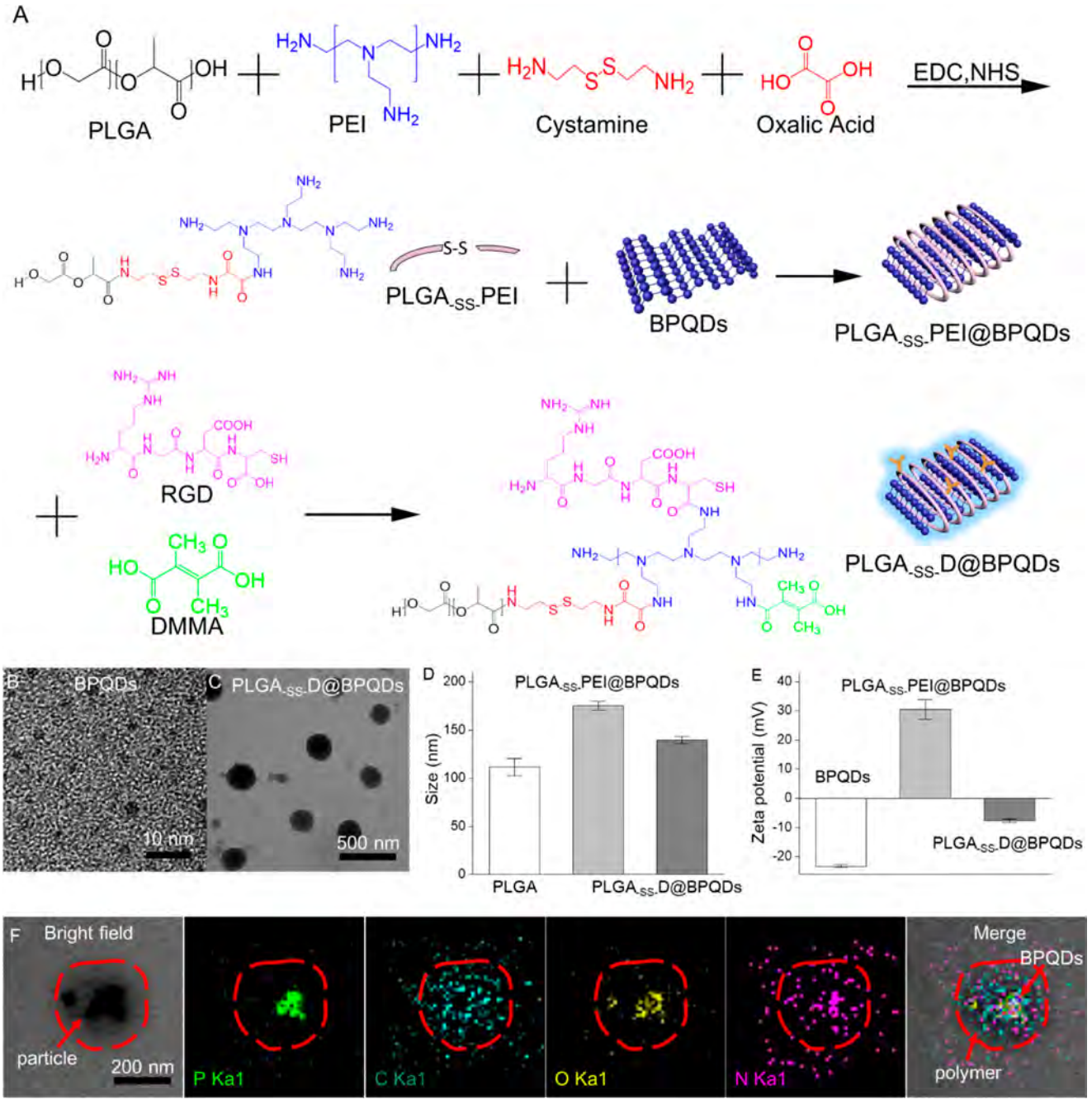

Figure 1. Characterization of PLGA$_{-SS-}$D@BPQDs: (A) Schematic illustrating the preparation of PLGA$_{-SS-}$D@BPQDs; (B, C) TEM images of the BPQDs and PLGA$_{-SS-}$D@BPQDs; (D) hydrodynamic size distribution of the PLGA, PLGA$_{-SS-}$PEI@BPQDs, and PLGA$_{-SS-}$D@BPQDs; (E) zeta potentials of the BPQDs, PLGA$_{-SS-}$PEI@BPQDs, and PLGA$_{-SS-}$D@BPQDs; (F) EDS mappings of PLGA$_{-SS-}$D@BPQDs.

endow the nanosystem with the surface charge-switching ability. Moreover, DMMA blocks cellular uptake in the nanosystem by neutralizing the positive charge of PEI before reaching tumor sites during blood circulation (pH 7.4).[34−36] Introduction of the targeting polypeptide peptide motif Arg-Gly-Asp-Gys (RGD) results in the RGD/integrin-mediated cancer-targeting ability and accurate site-specific release.[37−39] When the nanosystem is transported to tumor sites by blood circulation, the nanoparticles expand in response to the acidic tumor microenvironment (pH ≈ 6.8), and the amide linkages of DMMA are hydrolyzed, leading to DMMA dissociation from the nanosystem. Subsequently, the PEI layer exposed on the surface with positive charges increases cell uptake and the disulfide linkage between the semidegraded PLGA nanoparticles and PEI polymer is reduced by thiols *in vivo*, leading to responsive breakdown of the internal polymer layer and finally efficient release of the loaded BPQDs (Scheme 1). The *in vitro* and *in vivo* experiments demonstrate that the nanosystem with enhanced cancer targeting and multiple bioresponsiveness is indeed a highly efficient radiotherapy sensitizer boasting improved radiotherapy efficacy for human melanoma cells.

RESULTS AND DISCUSSION

Design and Preparation of PLGA$_{-SS-}$D@BPQDs. The sequentially triggered cancer-targeting nanosystem is prepared

DOI: 10.1021/acsnano.8b06483
ACS Nano 2018, 12, 12401−12415

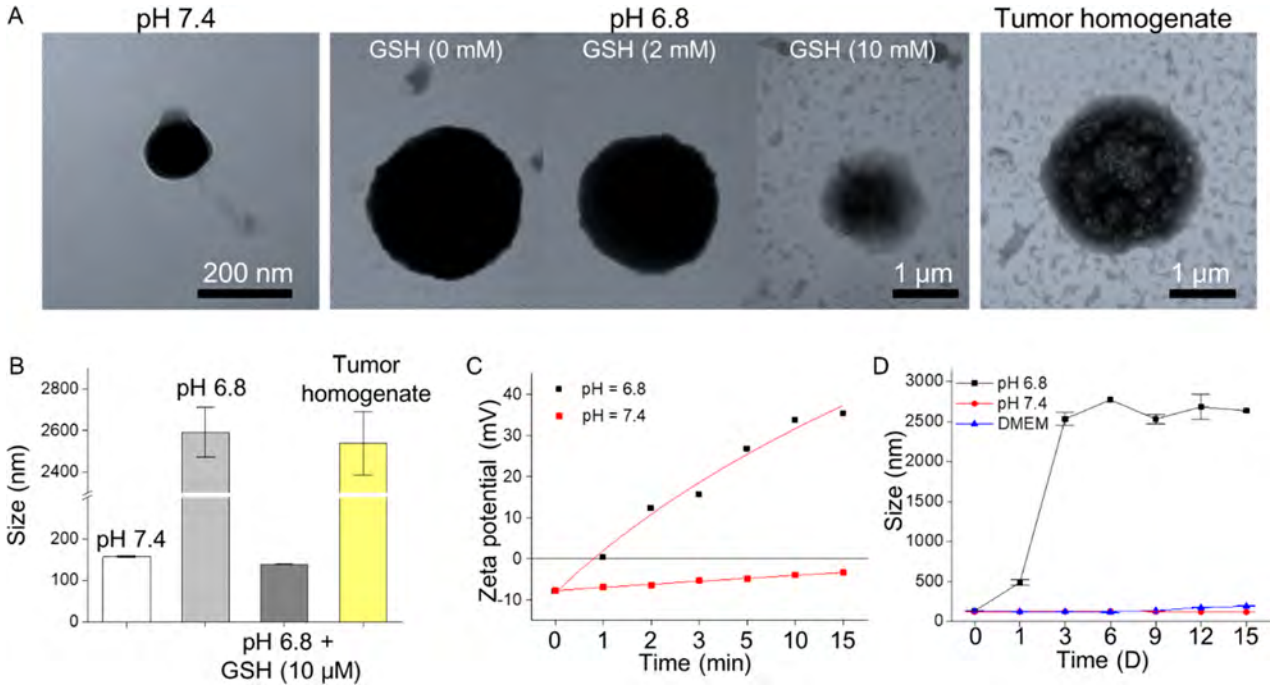

Figure 2. Surface charge switching ability of PLGA$_{-SS-}$D@BPQDs: (A) TEM image of the PLGA$_{-SS-}$D@BPQDs in the simulative tumor microenvironment; (B) pH-responsiveness of PLGA$_{-SS-}$D@BPQDs detected by the hydrodynamic size distribution; and (C) zeta potential and (D) stability of the PLGA$_{-SS-}$D@BPQDs.

by emulsion evaporation, and the PLGA-based nanoparticles with a core−shell structure are loaded with BPQDs to produce PLGA$_{-SS-}$D@BPQDs. The nanoparticles are conjugated with several layers of polymers in order to provide the precise bioresponsiveness in the biological environment. Considering the complex environmental influence and unspecific drug accumulation, cystamine and DMMA are introduced to the nanosystem. The bioresponsive cystamine with disulfide bond is bonded to PLGA, and PEI is connected with cystamine to introduce abundant amino functional groups to stabilize the PLGA nanoparticles. DMMA as a surface decorator endows the nanosystem with pH responsiveness to neutralize the positive charges of PEI and reduce cell uptake in normal tissues. Finally, RGD polypeptide as a cancer-targeting molecule is conjugated to PEI to enhance the selectivity between cancer cells and normal cells. Fabrication of the smart bioresponsive PLGA$_{-SS-}$D@BPQDs nanosystem is described in Figure 1A.

The PLGA$_{-SS-}$D@BPQDs are characterized by transmission electron microscopy (TEM), Zetasizer Nano-ZS particle analysis, ^{1}H NMR, Fourier transform infrared spectroscopy (FTIR), and X-ray photoelectron spectroscopy (XPS). The TEM images show that the size of the BPQDs is about 3 nm (Figure 1B). The PLGA$_{-SS-}$D@BPQDs have a spherical shape with an average size of about 150 nm, which is in accordance with the hydrated particle size (Figure 1C and D). Interestingly, the hydrated particle size of the PLGA$_{-SS-}$PEI@BPQDs is slightly bigger than PLGA$_{-SS-}$D@BPQDs, although the latter has additional layers of RGD and DMMA. PEI on the surface of PLGA$_{-SS-}$PEI@BPQDs has a high positive potential, and the particles are destabilized in an aqueous solution. The dendritic PEI spreads and is filled with water molecules, leading to a particle size increase to 175 nm. After introduction of DMMA, the surface potential of the particles tends to be balanced and the particle size is steady at about 140 nm. The zeta potentials in Figure 1E provide verification. PEI increases the zeta potentials of the nanosystem from −23 (BPQDs) to +30 mV (PLGA-PEI@BPQDs), boding well for dispersion and cellular uptake of the nanosystem due to the strong surface positive charge. DMMA, a polymeric molecule with a negative charge, is used to modify the nanoparticles to introduce the surface charge-switching ability and decrease the zeta potential to −7.78 mV in order to block cellular uptake of the nanosystem by normal cells. The chemical structure of PLGA$_{-SS-}$DMMA is determined by ^{1}H NMR (Figure S1), and the chemical shifts of PLGA, cystamine, PEI, DMMA, and RGD are shown in the ^{1}H NMR spectra. The characterization results confirm successful fabrication of PLGA$_{-SS-}$DMMA@BPQDs. In order to ascertain encapsulation of BPQDs by the polymer, energy-dispersive X-ray spectroscopy (EDS) maps are acquired from the PLGA$_{-SS-}$DMMA@BPQDs. Figure 1F reveals mainly carbon, oxygen, and nitrogen due to introduction of the diverse polymers, and phosphorus of the BPQDs is concentrated in the center of the particles. The results show that the BPQDs in the nanoparticles are protected and the PLGA$_{-SS-}$DMMA@BPQDs are successfully prepared.

Surface Charge-Switching Ability of PLGA$_{-SS-}$D@BPQDs. The surface charge-switching ability of PLGA$_{-SS-}$D@BPQDs is verified by TEM and Zetasizer Nano-ZS particle analysis. As shown in Figure 2A and B, the nanosystem with the negatively charged DMMA shell is stable in the simulated blood environment (PBS solution with a pH of 7.4). It has an average diameter of 157 nm, and the diameter increases to 2581 nm in the simulated tumor microenvironment (pH = 6.8). The results are similar to those of the particles incubated in the tumor homogenate (2539 nm). At a large concentration of GSH, the size of the expanded nanoparticles decreases to 139 nm due to deoxidization of the disulfide bond between PLGA and PEI by GSH. Figure 2C shows that the surface potential on the nanoparticles changes from −7.8 mV to +35.5

DOI: 10.1021/acsnano.8b06483
ACS Nano 2018, 12, 12401−12415

mV within 10 min in PBS at a pH of 6.8. The high positive potential benefits cellular uptake after the nanoparticles enter the acidic tumor microenvironment. The long-term stability experiment presented in Figure 2D shows that the size of the nanoparticles remains stable, below 200 nm in PBS (pH = 7.4) and DMEM with 10% fetal bovine serum (FBS) for 15 days. However, in the weakly acidic PBS (pH 6.8), the nanoparticles swell to 2530 nm in 3 days. Because the polymer is unstable under the weakly acidic condition (pH = 6.8), the DMMA decomposes from the particles, the side chains of PEI expand, and the PLGA core is exposed and filled with the acidic medium. Hence, the polymer nanoparticles swell from the nanometer to micrometer scale, thus facilitating BOQD release from the nanosystems. All in all, the PLGA$_{-SS-}$D@BPQDs with the surface charge switchable ability responds to the acidic tumor microenvironment very well.

Bioresponsiveness of PLGA$_{-SS-}$D@BPQDs. To verify the thiol-bioresponsiveness of the nanosystem originating from the disulfide bond between PLGA and PEI, a series of experiments were performed to detect the charge of the disulfide bond and sulfhydryl. As shown in Figure 3A, PLGA$_{-SS-}$DMMA is

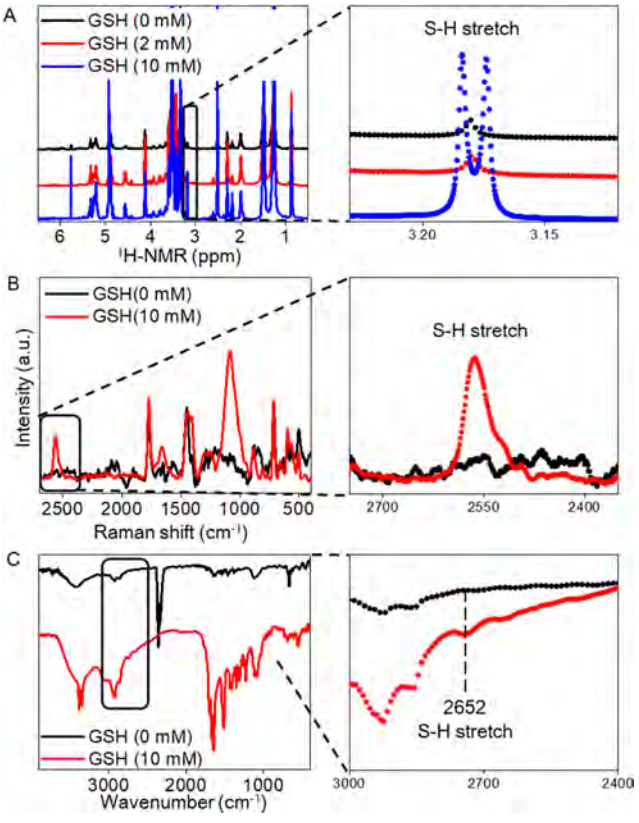

Figure 3. Bioresponsiveness of PLGA$_{-SS-}$D@BPQDs: (A) ^{1}H NMR of the PLGA$_{-SS-}$D@BPQDs incubated with GSH (0, 2, and 10 mM); (B) Raman scattering and (C) FTIR spectra of the PLGA$_{-SS-}$D@BPQDs incubated with GSH (0 and 10 mM).

prepared and dispersed in GSH solutions with different concentrations (0, 2, and 10 mM). A chemical shift of sulfhydryl at 3.17 ppm is observed from the ^{1}H NMR spectrum of PLGA$_{-SS-}$DMMA with 10 mM GSH, indicating that the disulfide bond of PLGA$_{-SS-}$DMMA is deoxidized by the large amount of GSH (10 mM) and sulfhydryl generated. Generation of the disulfide bond in PLGA$_{-SS-}$DMMA in GSH (10 mM) is corroborated by Raman scattering spectroscopy, and PLGA$_{-SS-}$DMMA with GSH (10 mM) shows a prominent peak at 2562 cm^{-1}, corresponding to S−H stretching (Figure 3B). The FTIR spectra in Figure 3C are consistent, and the peak at 2652 cm^{-1} is assigned to −S−H of the disulfide bond deoxidized by GSH. XPS, an important method to monitor reduction of a disulfide bond,[40,41] reveals binding energies of −S−H and −S−S− at 163 and 167 eV, respectively, thus providing evidence that the disulfide bond exists in the PLGA$_{-SS-}$DMMA. Compared to the polymer with 10 mM GSH in Figure 4B, this shift corresponds to a binding energy of −S−H at 163 eV, verifying that the disulfide bond is deoxidized to sulfhydryl by GSH. These results demonstrate introduction of cystamine, which provides the thiol-bioresponsiveness in the nanosystem.

Stability of PLGA$_{-SS-}$D@BPQDs. Since fast degradation of bare BPQDs is a major concern under physiological conditions, the stability of PLGA$_{-SS-}$D@BPQDs is compared to that of bare BPQDs. The bare BPQDs and PLGA$_{-SS-}$D@BPQDs are dispersed in water at the same concentration (5 mg/mL), and the optical absorption is examined. As shown in Figure 5A−C, the absorption intensity at 400 nm of the bare BPQD solution decreases gradually to 38% after 8 days (Figure 5A), but that of the PLGA$_{-SS-}$D@BPQDs does not change under the same conditions (100%) (Figure 5B). On the other hand, under weakly acidic conditions (pH = 6.8), the color of the PLGA$_{-SS-}$D@BPQDs fades gradually and the corresponding absorption intensity diminishes slowly to 56.7% of the original value (Figure 5C) on account of hydrolysis of the amide linkage between DMMA and PEI at acidic pH.

More experiments are performed to investigate the bioresponsive release of the loaded BPQDs from the PLGA$_{-SS-}$D@BPQDs. As shown in Figure 5D, the release rate of BPQDs is just 17.9% after incubation for 36 h in neutral PBS (pH = 7.4) to simulate normal blood. In comparison, accelerated release is observed when the PLGA$_{-SS-}$D@BPQDs are incubated with a larger concentration of GSH. At a pH of 7.4 with 10 mM GSH, the release rate is 45.1%, and at a pH of 6.8, it is 64.3%. Incubation of PLGA$_{-SS-}$D@BPQDs in acidic PBS in the presence of a large concentration of GSH (pH 6.8, 10 mM GSH) simulates the tumor environment better. The higher release rate of BPQDs is evidenced by burst release of BPQDs of 89.5% of the original value at the 4 h time point and complete release after incubation for 36 h. It is possible that the BPQD release from the nanosystem is controlled by a sequentially triggered delivery process. In the first stage, the DMMA shell of PLGA$_{-SS-}$D@BPQDs decomposes from the particles because the amido bond is unstable in the acidic condition. Then the PLGA$_{-SS-}$PEI particles swell to micrometer scale and the disulfide bond connecting PLGA and PEI is exposed and broken by GSH. Finally the polymer nanoparticles generate lots of cracks and holes, and the BPQDs release from nanosystems in the tumor tissue. The data confirm that the nanosystem is able to protect the BPQDs from degradation during circulation in normal body blood, but targeted drug release and accumulation are observed when they reach the tumor.

Radiotherapy Effects of PLGA$_{-SS-}$D@BPQDs Together with X-ray. Biocompatibility is crucial, and the radiotherapy sensitization efficiency of the PLGA$_{-SS-}$D@BPQDs is evaluated *in vitro* (Table 1). The A375 cancer cells, HeLa cancer cells, and L02 normal cells are incubated with Au nanoparticles (AuNPs), BPQDs, and PLGA$_{-SS-}$D@BPQDs (0−100 μg/mL) before exposure to 2 Gy of X-ray irradiation. The single

DOI: 10.1021/acsnano.8b06483
ACS Nano 2018, 12, 12401−12415

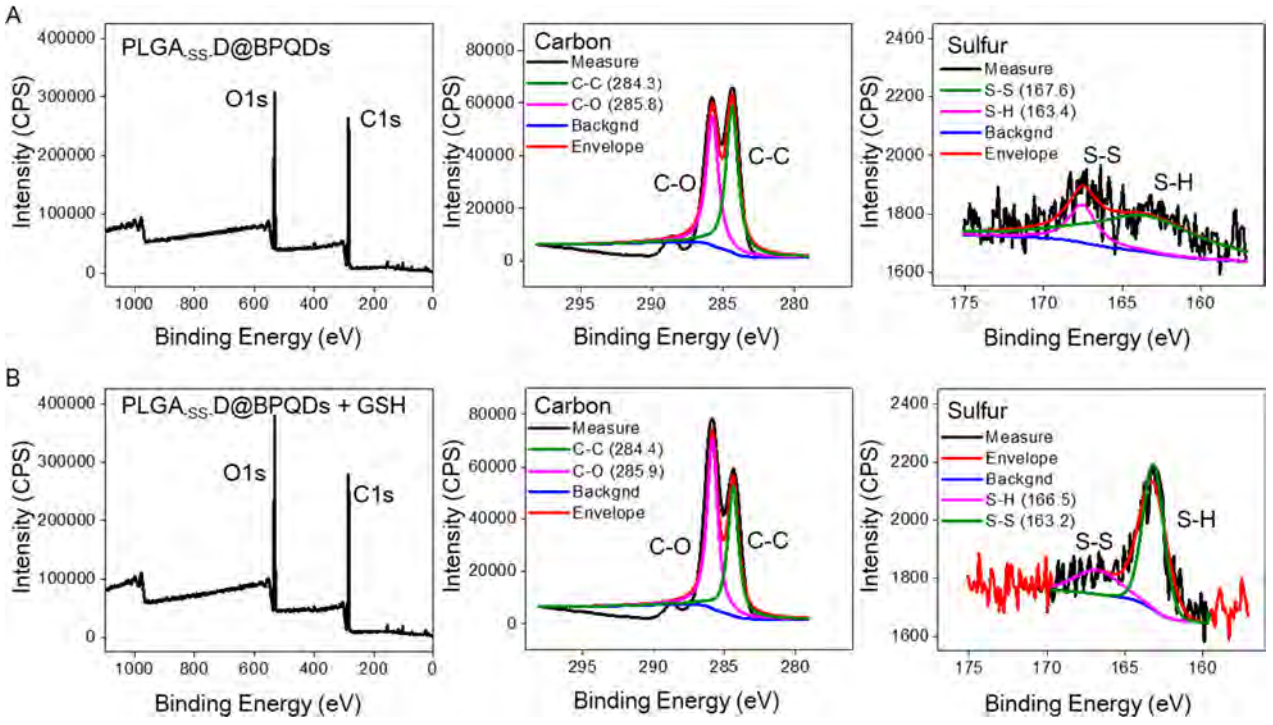

Figure 4. XPS analysis of the nanosystem: XPS spectra of PLGA$_{SS}$D@BPQDs incubated with (A) 0 and (B) 10 mM GSH.

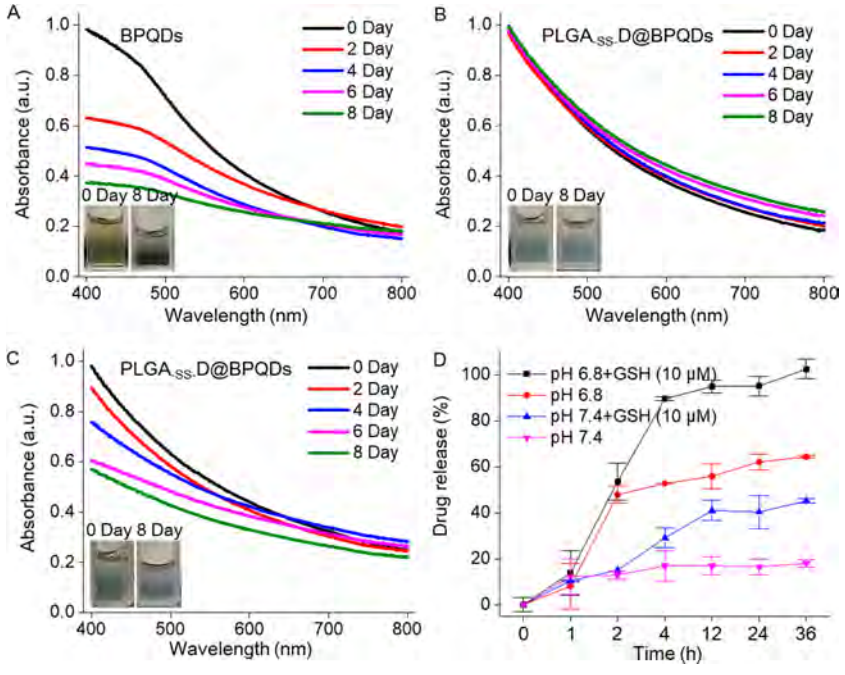

Figure 5. Stability of PLGA$_{SS}$D@BPQDs: (A) Absorption of the BPQDs and (B) PLGA$_{SS}$D@BPQDs in PBS at pH 7.4; (C) absorption of the PLGA$_{SS}$D@BPQDs in PBS at pH 6.8; (D) drug release observed from the PLGA$_{SS}$D@BPQDs under different conditions.

treatment of PLGA$_{SS}$D@BPQDs shows modest anticancer ability compared to BPQDs. However, the PLGA$_{SS}$D@BPQDs attenuate the cytotoxicity of BPQDs against L02 cells, as illustrated by the smaller IC_{50} value of 25.94 μg/mL (3.29 μg/mL of BPQDs treatment). The cytotoxicity of PLGA$_{SS}$D@BPQDs with X-ray (3.03 μg/mL) is 10 times lower than that of the BPQDs (0.31 μg/mL) against L02 cells, and the safe index of PLGA$_{SS}$D@BPQDs with X-ray is 11.65 (0.69 of BPQDs and X-ray cotreatment). The results demonstrate that PLGA$_{SS}$D@BPQDs are safer and more suitable than bare BPQDs in cancer therapy.

To assess the sensitization efficiency, AuNPs as a traditional radiosensitizer are compared to BPQDs and PLGA$_{SS}$D@BPQDs in radiotherapy sensitization. After X-ray irradiation, the AuNPs display general cytotoxicity for A375, HeLa, and L02 cells, and the IC_{50} values are 5.10, 11.03, and 11.30 μg/mL. In comparison, the IC_{50} values after the combined treatment of PLGA$_{SS}$D@BPQDs and X-ray radiation against A375 and HeLa cells improve by about 14 times to 0.26 and

DOI: 10.1021/acsnano.8b06483
ACS Nano 2018, 12, 12401−12415

Table 1. Cytotoxicity of the PLGA$_{SS}$D@BPQDs after Incubation in A375, HeLa, and L02 Cells for 72 h

IC_{50} (μg/mL)	A375	HeLa	L02[a]	safe index[b]
AuNPs	63.72 ± 4.45	44.13 ± 1.32	50.85 ± 3.05	1.15
BPQDs	2.79 ± 0.01	2.83 ± 0.01	3.29 ± 0.20	1.17
PLGA$_{SS}$D@BPQDs	3.87 ± 0.03	3.53 ± 0.21	25.94 ± 1.03	7.34
AuNPs + X-ray	5.10 ± 0.15	11.03 ± 1.21	11.30 ± 0.11	2.22
BPQDs + X-ray	0.45 ± 0.03	0.46 ± 0.02	0.31 ± 0.01	0.69
PLGA$_{SS}$D@BPQDs + X-ray	0.26 ± 0.01	0.27 ± 0.01	3.03 ± 0.29	11.65

[a]Normal cells. [b]Safe index = IC_{50}(L02)/IC_{50}(A375).

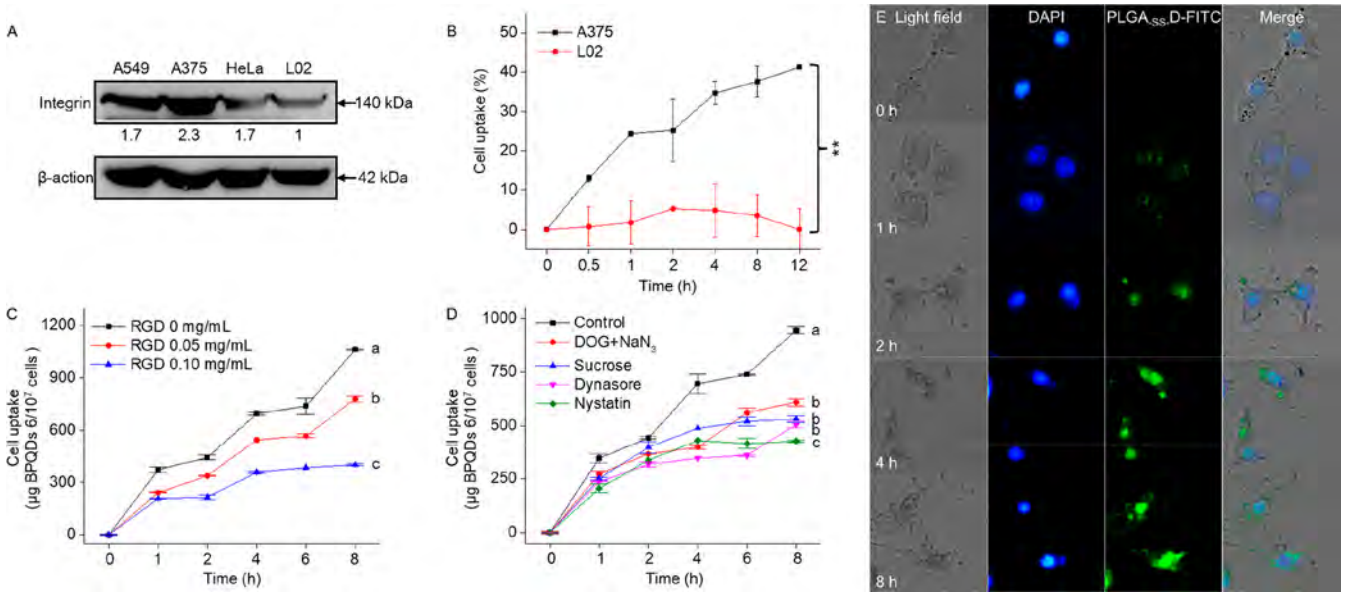

Figure 6. Selectivity of PLGA$_{SS}$D@BPQDs: (A) Expression level of integrin in A549, A375, HeLa, and L02 cells. β-Actin is used as the loading control; (B) cell uptake of the PLGA$_{SS}$D@BPQDs between A375 cancer cells and L02 normal cells; (C) cell uptake efficacy of PLGA$_{SS}$D@BPQDs (2 μg/mL) in A375 cancer cells after incubation with different concentrations of RGD for 2 h; (D) cell uptake efficacy PLGA$_{SS}$D@BPQDs (2 μg/mL) in A375 cancer cells after incubation with different endocytosis inhibitors; (E) intracellular trafficking of PLGA$_{SS}$D-FITC in A375 cells for an observation period of 8 h. Each value represents means ± SD (n = 3). Bars with different characteristics are statistically different at the P < 0.05 level.

0.27 μg/mL, and both have 2 times higher cytotoxicity than of BPQDs. The interaction between X-ray and PLGA$_{SS}$D@BPQDs is investigated by isobologram analysis, and as shown in Figure S2, the data points of the combined PLGA$_{SS}$D@BPQDs and X-ray treatment are below the line that defines the additive interaction, thus demonstrating the excellent performance of PLGA$_{SS}$D@BPQDs as a radiosensitizer.

Selective Cellular Uptake of PLGA$_{SS}$D@BPQDs. As the PLGA$_{SS}$D@BPQDs nanosystem is conjugated with RGD, it should possess good selectivity between cancer cells and normal cells due to RGD/integrin-mediated targeting. The expressions of integrin in cancerous A549, A375, and HeLa cells as well as a normal L02 cell are investigated by Western blotting. As shown in Figure 6A, the expression levels of the integrin in A375 cells are the highest, while the L02 normal cells show the lowest expression of integrin. The differential expression of integrin antigen between cancer and normal cells possibly promotes the selectivity of cancer cells *in vitro*. The cell uptake experiments (Figure 6B) reveal that the PLGA$_{SS}$D@BPQDs have over 10-fold expectant selectivity in A375 cancer cells compared to L02 normal cells. The cellular uptake efficacy of PLGA$_{SS}$D@BPQDs increases to 25.2% after 1 h and increases gradually to 41.2% after 12 h for A375 cells. In contrast, the cellular uptake efficiency of PLGA$_{SS}$D@BPQDs in L02 cells is below 10% in the 12 h treatment.

To study the role of RGD polypeptide on the selectivity of PLGA$_{SS}$D@BPQDs, the RGD competing assay is conducted (Figure 6C). Exposure of A375 cells to different concentrations of RGD reduces the cellular uptake efficiency of PLGA$_{SS}$D@BPQDs in a dose- and time-dependent manner. The cellular uptake of PLGA$_{SS}$DMMA@BPQDs is reduced from 1063 μg to 399 μg BPQDs 6/10^7 cells in the presence of 0.1 mg/mL RGD. To understand the internalization mode of PLGA$_{SS}$D@BPQDs, the endocytosis inhibitor blocking assay is performed. As shown in Figure 6D, the cellular uptake efficacy of PLGA$_{SS}$D@BPQDs in A375 cells decreases after incubation with various endocytosis inhibitors. In particular, pretreatment of cells with nystatin inhibits cellular uptake of PLGA$_{SS}$D@BPQDs from 944.7 to 425.9 μg BPQDs 6/10^7 cells, indicating that the nanosystem enters cells mainly *via* the caveolin-mediated pathway. Furthermore, the intracellular trafficking results show that the PLGA$_{SS}$D-FITC starts to enter A375 cells within 1 h, accumulates in lysosomes after 2 h, and translocates in the nucleus after 8 h (Figure 6E). These results disclose that RGD decoration enhances the endocytic uptake of PLGA$_{SS}$D@BPQDs through the caveolin-mediated pathway.

DOI: 10.1021/acsnano.8b06483
ACS Nano 2018, 12, 12401−12415

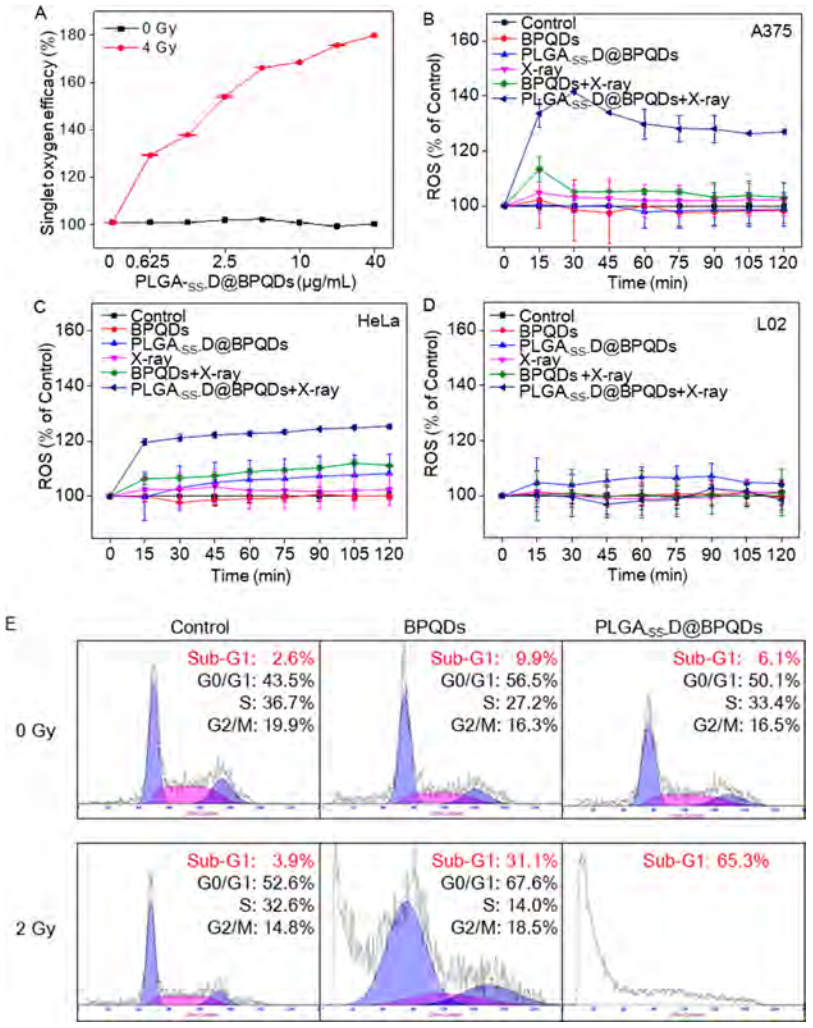

Figure 7. PLGA$_{SS}$D@BPQDs combines with X-ray to cause A375 cell apoptosis. (A) Radiotherapy sensitivity efficacy of the PLGA$_{SS}$D@BPQDs under X-ray irradiation. (B) Quantification of the intracellular ROS level in A375, (C) HeLa, and (D) L02 cells after treatment with the same concentrations of BPQDs and PLGA$_{SS}$D@BPQDs with X-ray (2 Gy). (E) Flow cytometric analysis of A375 cells treated with an equivalent concentration BPQDs and PLGA$_{SS}$D@BPQDs (0.5 μg/mL) together with X-ray (2 Gy) for 48 h.

Cancer Cell Apoptosis Induced by PLGA$_{SS}$D@BPQDs with X-ray. Enhanced generation of reactive oxygen species as an essential chemical signal causing DNA damage and apoptosis induction is regarded as a prime sensitization mechanism in cancer radiotherapy. Since the singlet oxygen ($^1O_2$) can be efficiently generated from BPQDs due to photodynamic effects, $^1O_2$ production from PLGA$_{SS}$D@BPQDs in response to X-ray exposure is assessed by monitoring the absorbance changes of the 1,3-diphenylisobenzofuran (DPBF) probe interacting with $^1O_2$. As shown in Figure 7A, the singlet oxygen efficiency of PLGA$_{SS}$D@BPQDs without illumination is relatively low and stable in the aqueous solution, but increases in a dose-dependent manner when exposed to X-ray (4 Gy). When the concentration of PLGA$_{SS}$D@BPQDs is increased to 40 μg/mL, the singlet oxygen efficacy of PLGA$_{SS}$D@BPQDs increases from 100% to 178%, demonstrating that PLGA$_{SS}$D@BPQDs enable efficient generation of singlet oxygen in response to X-ray irradiation. Based on the above results, BPQDs have potential radiosensitizing ability as the BPQDs produce singlet oxygen after X-ray irradiation, and the additional reactive oxygen species work in synergy with radiotherapy to accomplish better tumor radiotherapy sensitization effects. Overproduction of intracellular ROS in A375 (Figure 7B), HeLa (Figure 7C), and L02 (Figure 7D) cells is studied to support the radiosensitive property of BPQD. ROS generation induced by the combined treatment of PLGA$_{SS}$D@BPQDs and X-ray increases significantly in cancer cells but not in L02 normal cells, which exhibit limited cellular uptake of the nanosystem. In particular, the PLGA$_{SS}$D@BPQDs with X-ray exposure trigger more ROS generation in A375 cells than cells treated with the single nanosystem without radiation. For instance, the ROS content reaches the maximum value of 141.2% at 30 min before stabilization. Furthermore, the fluorescence images of ROS are shown in Figure S3. The A375 cells treated with BPQDs or PLGA$_{SS}$D@BPQDs exhibit ordinary production of ROS, but the fluorescence signal is obviously enhanced after X-ray irradiation, especially the cotreatment group of PLGA$_{SS}$D@BPQDs and X-ray. Previous studies have shown that high levels of ROS can induce cell apoptosis through DNA damage, which can be quantified by the proportion of Sub-G1 revealed by flow cytometry. Hence, flow cytometry is conducted to analyze the cell cycle distribution after the combined treatment of PLGA$_{SS}$D@BPQDs and X-ray. As shown in Figure 7E, in A375 cells treated with PLGA$_{SS}$D@BPQDs alone, the proportion of sub-G1 phase increases from 2.6% to 6.1%,

DOI: 10.1021/acsnano.8b06483
ACS Nano 2018, 12, 12401−12415

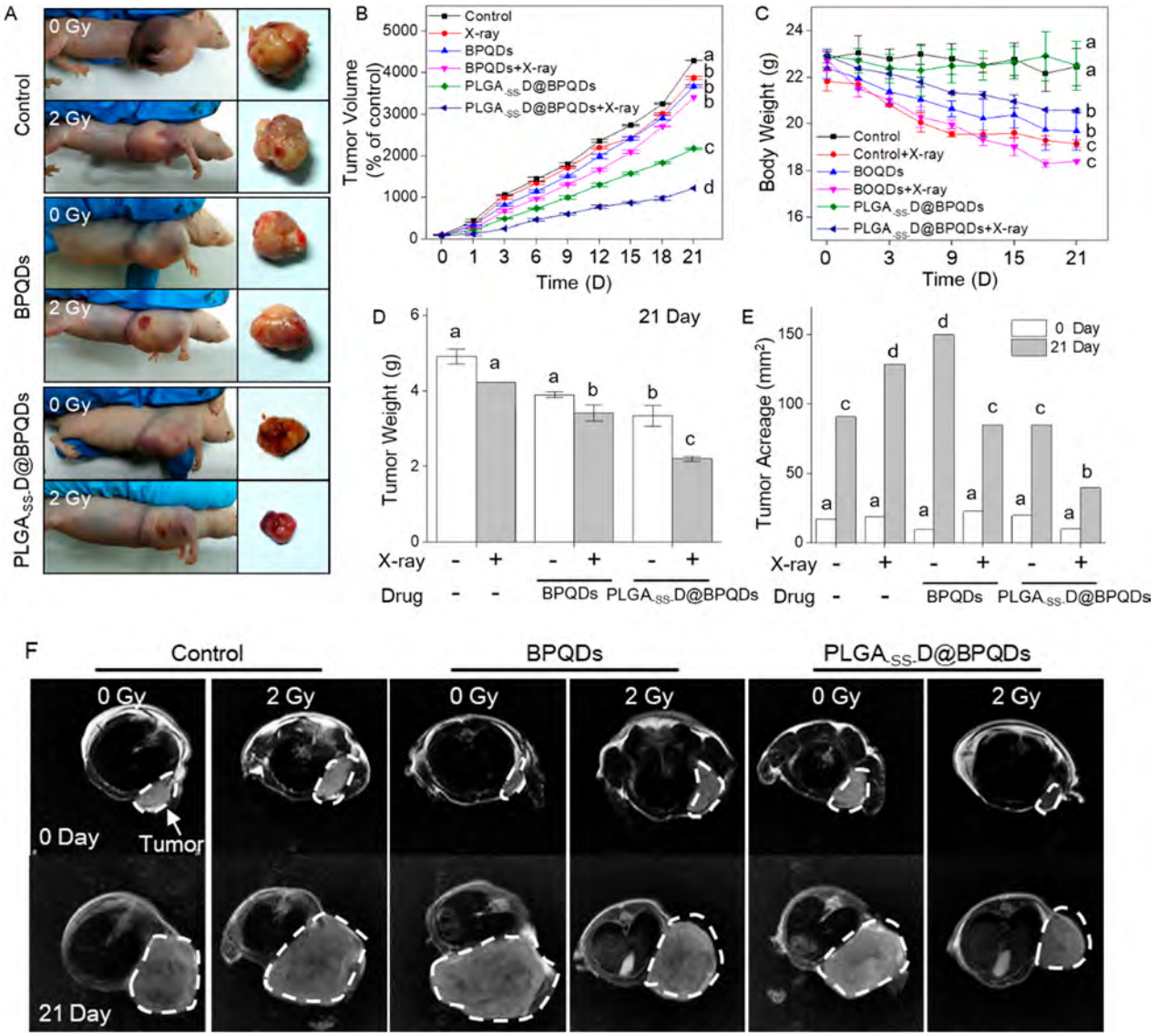

Figure 8. ***In vivo*** **radiotherapy efficacy and T2-weighted MR images of BPQDs and PLGA$_{SS}$D@BPQDs with X-ray (2 Gy) in A375-bearing mice: (A) Images of A375-bearing mice treated with BOQDs and PLGA$_{SS}$D@BPQDs with X-ray (2 Gy); (B) relative tumor volume and (D) tumor weight with PLGA$_{SS}$D@BPQDs and X-ray; (C) body weight of A375-bearing mice after treatment with PLGA$_{SS}$D@BPQDs and X-ray for 21 days; (F) images and (E) quantification of T2-weighted MR of A375-bearing mice after treatment with PLGA$_{SS}$D@BPQDs and X-ray. Each value represents means ± SD (n = 3). Bars with different characteristics are statistically different at the P < 0.05 level.**

but it increases sharply to 65.3% in cells cotreated with PLGA$_{SS}$D@BPQDs and X-ray. In contrast, the sub-G1 percentage of BPQDs with X-ray exhibits a modest onset from 9.9% to 31.1%. Hence, after X-ray irradiation, BPQDs have excellent radiosensitive properties, and singlet oxygen is generated to render tumor cells sensitive to X-ray. Cotreatment with PLGA$_{SS}$D@BPQDs and X-ray shows increased cytotoxicity against A375 cells due to the higher level of ROS-mediated apoptosis.

In Vivo **Radiotherapy Sensitivity Efficacy of PLGA$_{SS}$D@BPQDs in combination with X-ray in A375-Bearing Mice.** The *in vivo* radiotherapy sensitivity efficacy of PLGA$_{SS}$D@BPQDs and BPQDs is studied by intravenous (iv) injection using A375 subcutaneous transplanted tumor-bearing nude mice. As expected, the tumor size of the dissected tumors decreases significantly after the cotreatment after 21 days compared to the control (treated with saline), X-ray irradiation, BPQDs, BPQDs + X-ray, and PLGA$_{SS}$D@BPQDs groups (Figure 8A). The tumor volume of each group is quantified with a caliper, and as shown in Figure 8B, the relative tumor volume after the saline and X-ray treatment increases by 4279% and 3866%, respectively. Despite exhibiting strong anticancer activity on the cellular level, the cotreatment has no obvious inhibitory effect on tumor growth *in vivo,* as evidenced by the relative tumor volume increasing to 3404% on the 21st day. However, the treatment with PLGA$_{SS}$D@BPQDs and PLGA$_{SS}$D@BPQDs + X-ray reduces the relative tumor volume to 2168% and 1220%, respectively, showing excellent tumor suppressive effects. NMR imaging is carried out, and as shown in Figure 8D, the tumor weight after the PLGA$_{SS}$D@BPQDs + X-ray cotreatment decreases from 4.9 g to 2.2 g. The NMR images and histograms are consistent (Figure 8E and F). The weight of the nude mice is presented in Figure 8C. Radiotherapy reduces the body weight of mice, particularly cotreatment with BPQDs and X-ray, as evidenced by the body weight reduced from 22.7 g to

DOI: 10.1021/acsnano.8b06483
ACS Nano 2018, 12, 12401−12415

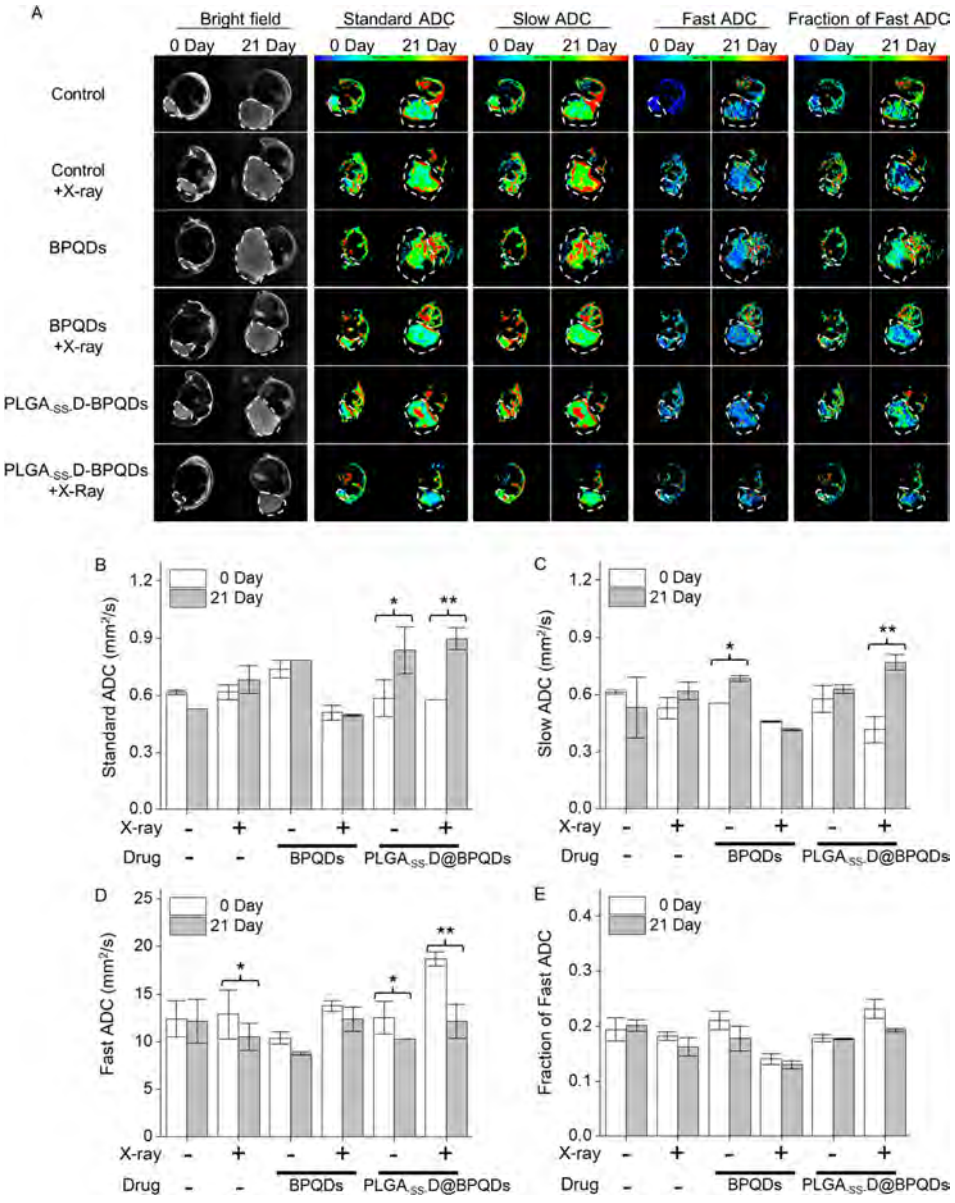

Figure 9. ***In vivo*** **magnetic resonance diffusion-weighted imaging analysis: (A) Diffuse weighted imaging analysis of nude mice after treatment with PLGA$_{SS}$D@BPQDs (20 μg/kg) and X-ray (2 Gy) for 21 days. (B, C, D, and E) Quantification of diffuse weighted imaging analysis. Each value represents means $\pm$ SD (n = 3). Bars with different characteristics are statistically different at the P < 0.05 level.**

18.4 g. In addition to showing enhanced radiosensitivity and tumor suppressive effect due to the tumor accumulation by active and passive targeting, effective prevention of premature drug leakage in blood circulation is accomplished using the cotreatment.

To verify cancer growth inhibition, NMR imaging is conducted to analyze the diffusion-weighted imaging (DWI) parameter. The parameter of standard ADC and slow ADC represent the cell activity in the region, whereas the parameter of fast ADC and fraction of fast ADC represent hemoperfusion in the region. As shown in Figure 9, the values of standard ADC and slow ADC decrease obviously after the treatment with PLGA$_{SS}$D@BPQDs, but the fast ADC value increases further, demonstrating the excellent radiotherapy sensitization effects of PLGA$_{SS}$D@BPQDs in tumor therapy.

In Vivo **Toxicity Evaluation.** To examine the potential side effects of PLGA$_{SS}$D@BPQDs *in vivo*, the main organs are collected from the mice and subjected to H&E staining. As shown in Figure 10 A, the main organs exhibit healthy and normal morphologies without impairment or inflammation after treatment with high concentrations of the PLGA$_{SS}$D@BPQDs. Moreover, blood indicators including glutamic oxalacetic transaminase (AST), urea nitrogen (BUN), creatine kinase (CK), and creatinine (CREA) (indices for liver and kidney function) are close to those of healthy mice after the treatment with PLGA$_{SS}$D@BPQDs (Figure 10B–E), certifying the biological safety *in vivo*.

CONCLUSION

A BPQDs-based radiosensitizing nanosystem is designed to accomplish high radiotherapy efficacy, low toxicity, and accurate tumor tissue localization through RGD targeting, surface charge switching, and bioresponsiveness. The PLGA$_{SS}$D@BPQDs accumulate in tumor tissues, and the DMMA shell decomposes under the weak acidic conditions at

DOI: 10.1021/acsnano.8b06483
ACS Nano 2018, 12, 12401–12415

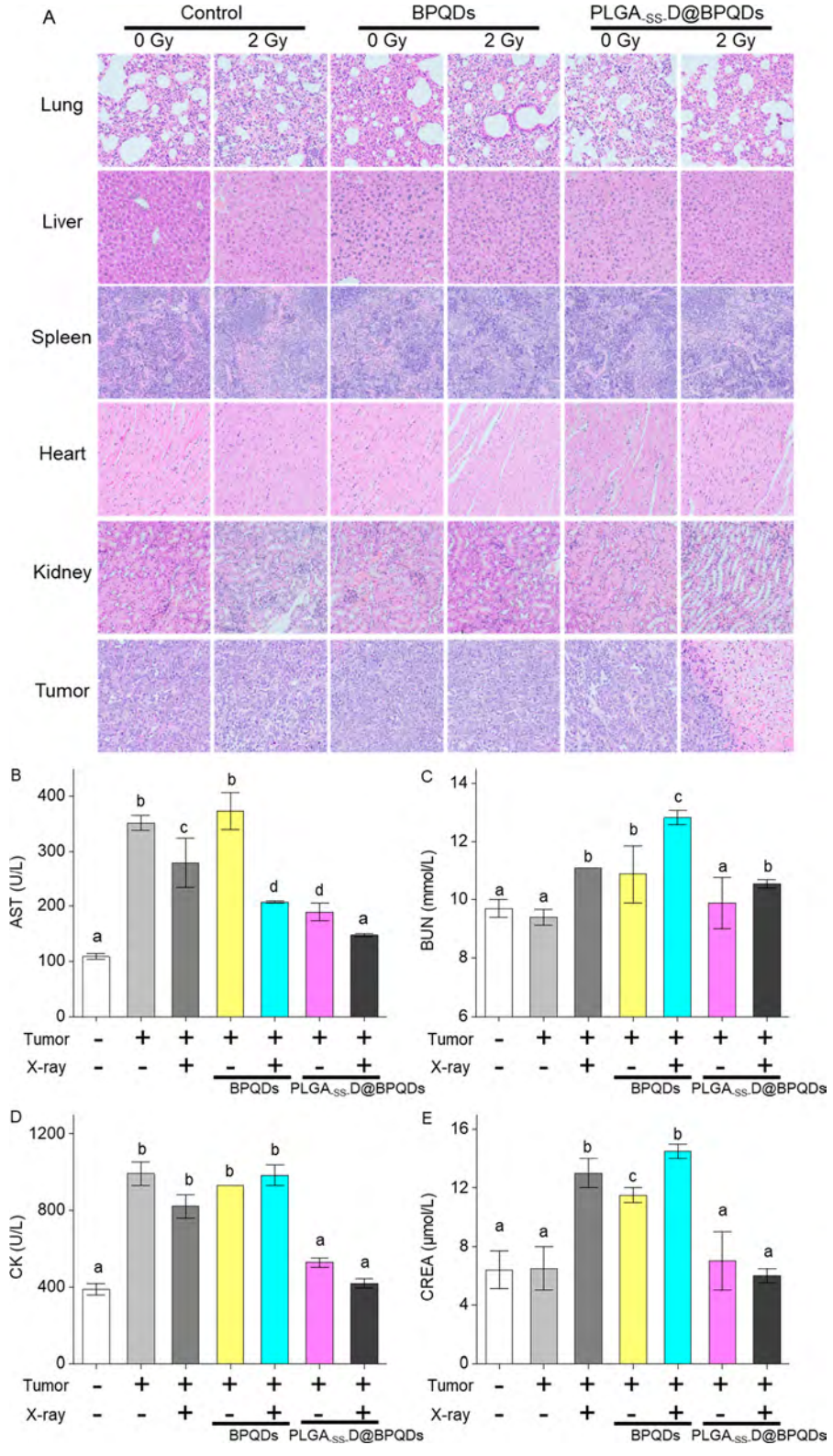

Figure 10. *In vivo* **toxicity evaluation: (A) H&E staining of the lung, liver, spleen, heart, kidney, and tumor after the combined treatment of PLGA$_{-SS-}$D@BPQDs (20 μg/kg) and X-ray (2 Gy) for 21 days. Histograms of the hematological analysis of (B) AST, (C) BUN, (D) CK, and (E) CREA in nude mice treated with PLGA$_{-SS-}$D@BPQDs (20 μg/kg) and X-ray (2 Gy) for 21 days. Each value represents means ± SD (n = 3). Bars with different characteristics are statistically different at the $P < 0.05$ level.**

tumor sites. The cellular uptake efficacy improves significantly with more surface charges, and the high concentration of GSH deoxidizes the disulfide bond of cystamine, resulting in release of BPQDs in the tumor region as an efficient radiosensitizing drug. X-ray irradiation triggers BPQDs to generate $^1O_2$ and inhibits cancer progression, and the treatment combining PLGA$_{-SS-}$D@BPQDs and X-ray activates $^1O_2$ overproduction to induce cancer cell apoptosis. As a class of radiosensitizer,

DOI: 10.1021/acsnano.8b06483
ACS Nano 2018, 12, 12401−12415

PLGA$_{-SS-}$D@BPQDs have several advantages: (1) excellent selectivity uptake of cancer cells with RGD-targeting molecules, (2) obvious surface charge-switching ability to support selective uptake, (3) specific release performance with bioresponsiveness controlled by the concentration of glutathione, and (4) higher radiotherapy efficiency and lower toxicity while using a low dose of X-ray. The results provide insights into cancer-targeting strategies. The bioresponsive nanosystem with the surface charge-switching ability constitutes a potent radiosensitizer with excellent radiotherapy sensitization efficacy and negligible toxic side effects.

EXPERIMENTAL SECTION

Materials. PLGA (LA:GA = 50:50, M_n = 13 000), oxalic acid, polyethylenimine (PEI, M_n = 10 000), cystamine, 2,3-dimethylmaleic anhydride (DMMA), oxalic acid, Arg-Gly-Asp-Cys (RGD), 1-(3-(dimethylamino)propyl)-3-ethylcarbodiimide hydrochloride (EDC), *N*-hydroxy succinimide (NHS), fluorescein isothiocyanate (FITC), Tween-80, thiazolyl blue tetrazolium bromide (MTT), and propidium iodide (PI) were purchased from Sigma-Aldrich. Black phosphorus quantum dots were synthesized by co-workers. Water used in all the experiments was distilled water (DW).

Preparation of PLGA$_{-SS-}$PEI@BPQDs. The BPQDs were synthesized by the method reported by our group previously,[42] and the PLGA$_{-SS-}$@BPQDs were prepared by emulsification evaporation.[43,44] The organic phase was prepared with 10 mg of PLGA, 20 μg of BPQDs, 1 mg of cystamine, 0.2 M EDC, and 0.2 M NHS and dispersed in 3 mL of acetone. The solution underwent ultrasonication until the BPQDs were uniformly dispersed. The organic phase was dropwise added to 10 mL of the Tween-80 aqueous solution (5 mg/mL) that included 1 mg of cystamine, 0.2 M EDC, and 0.2 M NHS. The mixture was stirred at room temperature. After 2 h, 1 mg of oxalic acid was added under stirring at 600 rpm/min for 4 h, and 10 mg of PEI was added and stirred overnight.

Preparation of PLGA$_{-SS-}$D@BPQDs. A 5 mg amount of RGD polypeptide and excess DMMA were added to the PLGA$_{-SS-}$PEI@BPQDs solution and stirred at 60 rpm/min. After 8 h, the product was dialyzed against a 100-fold volume of Milli-Q water (M_w 10 000) overnight.

Preparation of PLGA$_{-SS-}$D-FITC. A 10 mg amount of PLGA, 1 mg of cystamine, 0.2 M EDC, and 0.2 M NHS were dispersed in 3 mL of acetone. The organic phase was dropwise added to 10 mL of the Tween-80 aqueous solution (5 mg/mL). The mixture was stirred at room temperature. After 2 h, 1 mg of oxalic acid was added under stirring at 600 rpm/min for 4 h and 10 mg of PEI was added and stirred overnight. A 5 mg amount of FITC, 5 mg of RGD polypeptide, and excess DMMA were added to the PLGA$_{-SS-}$PEI@BPQDs solution and stirred at 60 rpm/min. After 8 h, the product was dialyzed against a 100-fold volume of Milli-Q water (M_w 10 000) overnight.

Characterization of PLGA$_{-SS-}$D@BPQDs. The morphology and structure of the synthesized PLGA$_{-SS-}$D@BPQDs were characterized by TEM,[45] EDS, FTIR, UV−vis−NIR spectrophotometry, a Zetasizer nano ZS analyzer (Malvern), NMR, ICP, Raman scattering, and XPS.[46] To measure the chemical structure of the samples, XPS, NMR, UV−vis−NIR, Raman scattering, and FTIR were used. The Zetasizer nano ZS analyzer was used to measure the size distribution and zeta potential, and the concentration of the BPQDs was determined by ICP analysis.

pH/Bioresponsive Properties of PLGA$_{-SS-}$D@BPQDs. The size and zeta potential of the nanoparticles were determined after PLGA$_{-SS-}$D@BPQDs were incubated in PBS with pH values at 7.4, 6.8, and 6.8 with GSH (10 mM) and tumor homogenate and monitored within 2 h using the Zetasizer Nano ZS particle analyzer.[47] The changes in the morphology of the nanosystem were observed by TEM.

The PLGA$_{-SS-}$D@BPQDs (50 mg) were separately suspended in 20 mL of GSH solution (0, 2, and 10 mM) and collected by lyophilization after dialysis. The bioresponsive properties were determined by XPS, NMR, FTIR, and Raman scattering.[48]

Stability of PLGA$_{-SS-}$D@BPQDs. The UV absorbance of the PLGA$_{-SS-}$D@BPQDs was monitored by UV−vis−NIR spectrophotometry to examine the stability.[23] A 5 mg amount of BPQDs and PLGA$_{-SS-}$D@BPQDs were dispersed in water at a pH of 7.0 or 6.8 in quartz cells and continuously monitored at time points of 0, 2, 4, 6, and 8 days. A 5 mg amount of PLGA$_{-SS-}$D@BPQDs was respectively suspended in 10 mL of PBS at 6.8 or 7.4 with GSH (0 and 10 mM) in glass tubes, and 300 μL of the mixture was collected by centrifugation; the supernatant was measured on a microplate reader at 450 nm.

Cell Culture and Viability Studies. All the cell lines were purchased from American Type Culture Collection (ATCC, Manassas, VA, USA), including A379 (human malignant melanoma cells), HeLa (human cervical carcinoma cells), and L02 (human hepatic cells). The cells were incubated in DMEM medium (Gibco, Paisley, UK) supplemented with FBS (Gibco) (10%), penicillin (Sigma-Aldrich) (100 units/mL), and streptomycin (Sigma-Aldrich) (50 units/mL) at 37 °C in a humidified incubator with 5% CO_2. The cytotoxicity of BPQDs, AuNPs, and PLGA$_{-SS-}$D@BPQDs was determined by the MTT assay.[1,49,50] A total of 2 × 10^3 cells/well of the A375, HeLa, and L02 cells were seeded on a 96-well plate with 100 μL of the growth medium. After 24 h, the cells were treated with BPQDs, AuNPs, and PLGA$_{-SS-}$D@BPQDs (0−100 μg/mL) either individually or combined with 2 Gy of X-ray for 72 h. The cells were incubated with 20 μL/well of the MTT solution for 4 h at 37 °C, and 150 μL of DMSO was used to replace the medium. Finally, the plates were shaken for 10 min to dissolve the formazan crystals, and the absorbance at 570 nm was measured on a microplate spectrophotometer (SpectroA max 250).

***In Vitro* Cellular Uptake Efficacy of PLGA$_{-SS-}$D@BPQDs.** The A375 and L02 cells at 1.2 × 10^6 cells/mL (2 mL) were seeded on a six-well plate for 24 h. The medium was replaced with fresh medium without phenol red, and 2 μg/mL of BPQDs and PLGA$_{-SS-}$D@BPQDs were added. The supernatant was collected, and the concentration of BPQDs was determined. To understand the mechanism of internalization, the RGD competing and blocking assay was prepared[51] and carried out similar to the cellular uptake experiments, except that the cells were incubated with RGD (0, 0.05, and 0.1 mg/mL) or endocytosis inhibitors (sodium azide (NaN_3) 10 mM, 2-deoxy-D-glucose (Sigma-Aldrich) 50 mM, sucrose 0.45 mM, Dynasore (Sigma-Aldrich) 80 μg/mL, and nystatin 10 μg/mL) before the treatment.

Cellular Fluorescence Localization of PLGA$_{-SS-}$D@BPQDs. The PLGA$_{-SS-}$DMMA-FITC was prepared to study the cellular fluorescence localization of the nanosystem.[52] A 2 mL amount of A375 cells at 4 × 10^4 cells/mL was seeded on a 2 cm dish and incubated with PLGA$_{-SS-}$DMMA-FITC (1 μg/mL). DAPI and Lysotracker were used to stain the cells before observation at 0.5 and 2 h. The cells were washed by PBS and observed by fluorescence microscopy (IX51, Olympus).

Measurement of Intracellular Reactive Oxygen Species Generation. The ability of singlet oxygen generation of PLGA$_{-SS-}$D@BPQDs in combination with X-ray was measured by the UV absorbance.[53−55] The PLGA$_{-SS-}$D@BPQDs (0, 0.625, 1.25, 2.5, 5, 10, 20, and 40 μg/mL) were added to a 96-well plate with DPBF in which the probes were quenched to regenerate singlet oxygen. After 4 Gy X-ray irradiation, the absorbance of DPBF at 410 nm was measured on a microplate spectrophotometer (SpectroA max 250). Generation of intracellular ROS was assessed by the 2,7-dichlorodihydrofluorescein diacetate (DCFH-DA) probe in various cells.[56] A 100 μL amount of A375, HeLa, and L02 cells at 2 × 10^6 cells/well were seeded on a 96-well plate for 24 h and treated with PLGA$_{-SS-}$D@BPQDs (2 μg/mL) and X-ray. The fluorescence intensity of ROS was determined under excitation by wavelengths of DCFH-DA at 488 and 525 nm.

Flow Cytometry. Flow cytometry was used to analyze the cell cycle treated with BPQDs and PLGA$_{-SS-}$D@BPQDs either individually or combined with X-ray.[57−59] A 6 mL amount of the A375 cells (2 × 10^4 cell/mL) was seeded on 6 cm dish. The cells were treated with 0.5 μg/mL of BPQDs and PLGA$_{-SS-}$D@BPQDs and irradiated with 2

DOI: 10.1021/acsnano.8b06483
ACS Nano 2018, 12, 12401−12415

Gy of X-ray. After culturing for 24 h, the cells were collected and fixed with 70% ethanol at −20 °C overnight. Finally, the cell cycle distribution was determined after staining with PI.

***In Vivo* Radiotherapy Effects and Toxicity of PLGA$_{-SS-}$D@BPQDs with X-ray.** The animal study was approved by the Animal Experimentation Ethics Committee of Jinan University. In brief, 1.5×10^7 A375 cells were used in the nude mice xenograft models. After the tumor grew to approximately 5 mm, the mice were irradiated with 2 Gy of X-ray after being intravenously injected with 20 μg/kg of BPQDs and PLGA$_{-SS-}$D@BPQDs for 21 d (1 time/2 day).[60] The test was conducted in test tubes based on the T2-weighted MRI relaxation measured on the 1.5 T Signa HDxt superconductor clinical MR system (GE Medical, Milwaukee, WI, USA).[61] The tumors and organs were fixed with formalin, and after H&E staining, they were observed under an optical microscope (Nikon ni-u, Japan).[62]

Statistical and Synergy Analysis. All the experiments were carried out at least in triplicate, and results were expressed as means ± SD. Differences between two groups were analyzed by the two-tailed Student's *t* test, and statistical analysis was performed using the SPSS statistical program version 13 (SPSS Inc., Chicago, IL, USA). The difference between three or more groups was analyzed by the one-way ANOVA, and a difference with $P < 0.05$ (*) or $P < 0.01$ (**) was considered statistically significant.

ASSOCIATED CONTENT

Supporting Information

The Supporting Information is available free of charge on the ACS Publications website at DOI: 10.1021/acsnano.8b06483.

^{1}H NMR of PLGA$_{-SS-}$DMMA (Figure S1); isobologram analysis of the synergistic antiproliferative effect of the combined application of X-ray and PLGA$_{-SS-}$D@BPQDs on A375 cells (Figure S2) (PDF)

AUTHOR INFORMATION

Corresponding Authors

*E-mail: xf.yu@siat.ac.cn (X. F. Yu).
*E-mail: tchentf@jnu.edu.cn (T. Chen).

ORCID

Xue-Feng Yu: 0000-0003-2566-6194
Tianfeng Chen: 0000-0001-6953-1342

Notes

The authors declare no competing financial interest.

ACKNOWLEDGMENTS

This work was supported by Natural Science Foundation of China (21877049), National Program for Support of Top-notch Young Professionals (W02070191), YangFan Innovative & Entrepreneur Research Team Project (201312H05), Fundamental Research Funds for the Central Universities, National Natural Science Foundation of China (51672305), Frontier Science Key Programs of Chinese Academy of Sciences (QYZDB-SSW-SLH034), and Hong Kong Research Grants Council (RGC) General Research Funds (GRF) Nos. CityU 11301215 and 11205617.

REFERENCES

(1) Yang, Y. H.; Xie, Q.; Zhao, Z. N.; He, L. Z.; Chan, L.; Liu, Y. X.; Chen, Y. L.; Bai, M. J.; Pan, T.; Qu, Y. N.; Ling, L.; Chen, T. F. Functionalized Selenium Nanosystem as Radiation Sensitizer of I-125 Seeds for Precise Cancer Therapy. *ACS Appl. Mater. Interfaces* **2017**, *9*, 25857−25869.

(2) Huang, Y. Y.; Luo, Y.; Zheng, W. J.; Chen, T. F. Rational Design of Cancer-Targeted BSA Protein Nanoparticles as Radiosensitizer to Overcome Cancer Radioresistance. *ACS Appl. Mater. Interfaces* **2014**, *6*, 19217−19228.

(3) Westhoff, M. A.; Marschall, N.; Grunert, M.; Karpel-Massler, G.; Burdach, S.; Debatin, K. M. Cell Death-Based Treatment of Childhood Cancer. *Cell Death Dis.* **2018**, *9*, 116.

(4) Song, G. S.; Ji, C. H.; Liang, C.; Song, X. J.; Yi, X.; Dong, Z. L.; Yang, K.; Liu, Z. TaOx Decorated Perfluorocarbon Nanodroplets as Oxygen Reservoirs to Overcome Tumor Hypoxia and Enhance Cancer Radiotherapy. *Biomaterials* **2017**, *112*, 257−263.

(5) Yang, X.; Yang, M. X.; Pang, B.; Vara, M.; Xia, Y. N. Gold Nanomaterials at Work in Biomedicine. *Chem. Rev.* **2015**, *115*, 10410−10488.

(6) Liu, P. D.; Huang, Z. H.; Chen, Z. W.; Xu, R. Z.; Wu, H.; Zang, F. C.; Wang, C. L.; Gu, N. Silver Nanoparticles: A Novel Radiation Sensitizer for Glioma? *Nanoscale* **2013**, *5*, 11829−11836.

(7) Detappe, A.; Lux, F.; Tillement, O. Pushing Radiation Therapy Limitations with Theranostic Nanoparticles. *Nanomedicine* **2016**, *11*, 997−999.

(8) Lux, F.; Sancey, L.; Bianchi, A.; Cremillieux, Y.; Roux, S.; Tillement, O. Gadolinium-Based Nanoparticles for Theranostic MRI-Radiosensitization. *Nanomedicine* **2015**, *10*, 1801−1815.

(9) Preihs, C.; Arambula, J. F.; Magda, D.; Jeong, H.; Yoo, D.; Cheon, J.; Siddik, Z. H.; Sessler, J. L. Recent Developments in Texaphyrin Chemistry and Drug Discovery. *Inorg. Chem.* **2013**, *52*, 12184−12192.

(10) Jayaraman, V.; Bhavesh, G.; Chinnathambi, S.; Ganesan, S.; Aruna, P. Synthesis and Characterization of Hafnium Oxide Nanoparticles for Bio-Safety. *Mater. Express* **2014**, *4*, 375−383.

(11) Stewart, C.; Konstantinov, K.; McDonald, M.; Bogusz, K.; Cardillo, D.; Oktaria, S.; Shi, D. Q.; Lerch, M.; Devers, T.; Corde, S.; Rosenfeld, A.; Tehei, M. Engineering of Bismuth Oxide Nanoparticles to Induce Differential Biochemical Activity in Malignant and Nonmalignant Cells. *Part. Part. Syst. Char.* **2014**, *31*, 960−964.

(12) Ma, P. A.; Xiao, H. H.; Yu, C.; Liu, J. H.; Cheng, Z. Y.; Song, H. Q.; Zhang, X. Y.; Li, C. X.; Wang, J. Q.; Gu, Z.; Lin, J. Enhanced Cisplatin Chemotherapy by Iron Oxide Nanocarrier-Mediated Generation of Highly Toxic Reactive Oxygen Species. *Nano Lett.* **2017**, *17*, 928−937.

(13) Hauser, A. K.; Mitov, M. I.; Daley, E. F.; McGarry, R. C.; Anderson, K. W.; Hilt, J. Z. Targeted Iron Oxide Nanoparticles for the Enhancement of Radiation Therapy. *Biomaterials* **2016**, *105*, 127−135.

(14) Meidanchi, A.; Akhavan, O.; Khoei, S.; Shokri, A. A.; Hajikarimi, Z.; Khansari, N. ZnFe2O4 Nanoparticles as Radiosensitizers in Radiotherapy of Human Prostate Cancer Cells. *Mater. Sci. Eng., C* **2015**, *46*, 394−399.

(15) Juzenas, P.; Chen, W.; Sun, Y. P.; Coelho, M. A. N.; Generalov, R.; Generalova, N.; Christensen, I. L. Quantum Dots and Nanoparticles for Photodynamic and Radiation Therapies of Cancer. *Adv. Drug Delivery Rev.* **2008**, *60*, 1600−1614.

(16) Kleinauskas, A.; Rocha, S.; Sahu, S.; Sun, Y. P.; Juzenas, P. Carbon-Core Silver-Shell Nanodots as Sensitizers for Phototherapy and Radiotherapy. *Nanotechnology* **2013**, *24*, 325103.

(17) Hernandez-Rivera, M.; Kumar, I.; Cho, S. Y.; Cheong, B. Y.; Pulikkathara, M. X.; Moghaddam, S. E.; Whitmire, K. H.; Wilson, L. J. High-Performance Hybrid Bismuth-Carbon Nanotube Based Contrast Agent for X-ray CT Imaging. *ACS Appl. Mater. Interfaces* **2017**, *9*, 5709−5716.

(18) Zhao, D.; Sun, X.; Tong, J.; Ma, J.; Bu, X.; Xu, R.; Fan, R. A Novel Multifunctional Nanocomposite C225-Conjugated Fe_3O_4/Ag Enhances the Sensitivity of Nasopharyngeal Carcinoma Cells to Radiotherapy. *Acta Biochim. Biophys. Sin.* **2012**, *44*, 678−684.

(19) Klein, S.; Kizaloglu, M.; Portilla, L.; Park, H.; Rejek, T.; Hummer, J.; Meyer, K.; Hock, R.; Distel, L. V. R.; Halik, M.; Kryschi, C. Enhanced *In Vitro* Biocompatibility and Water Dispersibility of Magnetite and Cobalt Ferrite Nanoparticles Employed as ROS Formation Enhancer in Radiation Cancer Therapy. *Small* **2018**, *14*, 1704111.

DOI: 10.1021/acsnano.8b06483
ACS Nano 2018, 12, 12401−12415

(20) Klein, S.; Sommer, A.; Distel, L. V. R.; Hazemann, J. L.; Kroner, W.; Neuhuber, W.; Muller, P.; Proux, O.; Kryschi, C. Superparamagnetic Iron Oxide Nanoparticles as Novel X-ray Enhancer for Low-Dose Radiation Therapy. *J. Phys. Chem. B* **2014**, *118*, 6159−6166.
(21) Klein, S.; Sommer, A.; Distel, L. V. R.; Neuhuber, W.; Kryschi, C. Superparamagnetic Iron Oxide Nanoparticles as Radiosensitizer *via* Enhanced Reactive Oxygen Species Formation. *Biochem. Biophys. Res. Commun.* **2012**, *425*, 393−397.
(22) Yi, Y.; Yu, X. F.; Zhou, W. H.; Wang, J. H.; Chu, P. K. Two-Dimensional Black Phosphonts: Synthesis, Modification, Properties, and Applications. *Mater. Sci. Eng., R* **2017**, *120*, 1−33.
(23) Shao, J. D.; Xie, H. H.; Huang, H.; Li, Z. B.; Sun, Z. B.; Xu, Y. H.; Xiao, Q. L.; Yu, X. F.; Zhao, Y. T.; Zhang, H.; Wang, H. Y.; Chu, P. K. Biodegradable Black Phosphorus-Based Nanospheres for *In Vivo* Photothermal Cancer Therapy. *Nat. Commun.* **2016**, *7*, 12967.
(24) Chen, W. S.; Ouyang, J.; Liu, H.; Chen, M.; Zeng, K.; Sheng, J. P.; Liu, Z. J.; Han, Y. J.; Wang, L. Q.; Li, J.; Deng, L.; Liu, Y. N.; Guo, S. J. Black Phosphorus Nanosheet-Based Drug Delivery System for Synergistic Photodynamic/Photothermal/Chemotherapy of Cancer. *Adv. Mater.* **2017**, *29*, 1603864.
(25) Tao, W.; Zhu, X. B.; Yu, X. H.; Zeng, X. W.; Xiao, Q. L.; Zhang, X. D.; Ji, X. Y.; Wang, X. S.; Shi, J. J.; Zhang, H.; Mei, L. Black Phosphorus Nanosheets as A Robust Delivery Platform for Cancer Theranostics. *Adv. Mater.* **2017**, *29*, 1603276.
(26) Zhou, W. H.; Cui, H. D.; Ying, L. M.; Yu, X. F. Enhanced Cytosolic Delivery and Release of CRISPR/Cas9 by Black Phosphorus Nanosheets for Genome Editing. *Angew. Chem., Int. Ed.* **2018**, *57*, 10268−10272.
(27) Zhao, Y. T.; Tong, L. P.; Li, Z. B.; Yang, N.; Fu, H. D.; Wu, L.; Cui, H. D.; Zhou, W. H.; Wang, J. H.; Wang, H. Y.; Chu, P. K.; Yu, X. F. Stable and Multifunctional Dye-Modified Black Phosphorus Nanosheets for Near-Infrared Imaging-Guided Photothermal Therapy. *Chem. Mater.* **2017**, *29*, 7131−7139.
(28) Panyam, J.; Labhasetwar, V. Biodegradable Nanoparticles for Drug and Gene Delivery to Cells and Tissue. *Adv. Drug Delivery Rev.* **2003**, *55*, 329−347.
(29) Owens, D. E.; Peppas, N. A. Opsonization, Biodistribution, and Pharmacokinetics of Polymeric Nanoparticles. *Int. J. Pharm.* **2006**, *307*, 93−102.
(30) Prasad, R.; Aiyer, S.; Chauhan, D. S.; Srivastava, R.; Selvaraj, K. Bioresponsive Carbon Nano-Gated Multifunctional Mesoporous Silica for Cancer Theranostics. *Nanoscale* **2016**, *8*, 4537−4546.
(31) Zhu, C. H.; Jung, S.; Luo, S. B.; Meng, F. H.; Zhu, X. L.; Park, T. G.; Zhong, Z. Y. Co-Delivery of siRNA and Paclitaxel into Cancer Cells by Biodegradable Cationic Micelles Based on PDMAEMA-PCL-PDMAEMA Triblock Copolymers. *Biomaterials* **2010**, *31*, 2408−2416.
(32) Xia, T. A.; Kovochich, M.; Liong, M.; Meng, H.; Kabehie, S.; George, S.; Zink, J. I.; Nel, A. E. Polyethyleneimine Coating Enhances the Cellular Uptake of Mesoporous Silica Nanoparticles and Allows Safe Delivery of siRNA and DNA Constructs. *ACS Nano* **2009**, *3*, 3273−3286.
(33) Yang, L. Y.; Li, W. Y.; Huang, Y. Y.; Zhou, Y. L.; Chen, T. F. Rational Design of Cancer-Targeted Benzoselenadiazole by RGD Peptide Functionalization for Cancer Theranostics. *Macromol. Rapid Commun.* **2015**, *36*, 1559−1565.
(34) Wang, C.; Cheng, L.; Liu, Y. M.; Wang, X. J.; Ma, X. X.; Deng, Z. Y.; Li, Y. G.; Liu, Z. Imaging-Guided pH-Sensitive Photodynamic Therapy Using Charge Reversible Upconversion Nanoparticles under Near-Infrared Light. *Adv. Funct. Mater.* **2013**, *23*, 3077−3086.
(35) Zhao, X.; Wei, Z.; Zhao, Z.; Miao, Y.; Qiu, Y.; Yang, W.; Jia, X.; Liu, Z.; Hou, H. Design and Development of Graphene Oxide Nanoparticle/Chitosan Hybrids Showing pH-Sensitive Surface Charge-Reversible Ability for Efficient Intracellular Doxorubicin Delivery. *ACS Appl. Mater. Interfaces* **2018**, *10*, 6608−6617.
(36) Zhou, Z. X.; Shen, Y. Q.; Tang, J. B.; Fan, M. H.; Van Kirk, E. A.; Murdoch, W. J.; Radosz, M. Charge-Reversal Drug Conjugate for Targeted Cancer Cell Nuclear Drug Delivery. *Adv. Funct. Mater.* **2009**, *19*, 3580−3589.
(37) Chen, Q.; Wang, X.; Wang, C.; Feng, L. Z.; Li, Y. G.; Liu, Z. Drug-Induced Self-Assembly of Modified Albumins as Nano-Theranostics for Tumor-Targeted Combination Therapy. *ACS Nano* **2015**, *9*, 5223−5233.
(38) Song, H. T.; Suh, J. S. Cancer-Targeted MR Molecular Imaging. *J. Korean Med. Assoc.* **2009**, *52*, 121−124.
(39) Fu, X. Y.; Yang, Y. H.; Li, X. L.; Lai, H. Q.; Huang, Y. Y.; He, L. Z.; Zheng, W. J.; Chen, T. F. RGD Peptide-Conjugated Selenium Nanoparticles: Antiangiogenesis by Suppressing VEGF-VEGFR2-ERK/AKT Pathway. *Nanomedicine* **2016**, *12*, 1627−1639.
(40) Bourg, M. C.; Badia, A.; Lennox, R. B. Gold-Sulfur Bonding in 2D and 3D Self-Assembled Monolayers: XPS Characterization. *J. Phys. Chem. B* **2000**, *104*, 6562−6567.
(41) Smart, R. S.; Skinner, W. M.; Gerson, A. R. XPS of Sulphide Mineral Surfaces: Metal-Deficient, Polysulphides, Defects and Elemental Sulphur. *Surf. Interface Anal.* **1999**, *28*, 101−105.
(42) Zhang, X.; Xie, H. M.; Liu, Z. D.; Tan, C. L.; Luo, Z. M.; Li, H.; Lin, J. D.; Sun, L. Q.; Chen, W.; Xu, Z. C.; Xie, L. H.; Huang, W.; Zhang, H. Black Phosphorus Quantum Dots. *Angew. Chem., Int. Ed.* **2015**, *54*, 3653−3657.
(43) Cirpanli, Y.; Bilensoy, E.; Calis, S.; Hincal, A. A. Stabilization of Camptothecin in PLGA Nanoparticles. *Eur. J. Pharm. Sci.* **2007**, *32*, S18−S19.
(44) Chan, L.; Huang, Y. Y.; Chen, T. Cancer-Targeted Tri-Block Copolymer Nanoparticles as Payloads of Metal Complexes to Achieve Enhanced Cancer Theranosis. *J. Mater. Chem. B* **2016**, *4*, 4517−4525.
(45) He, L. Z.; Huang, Y. Y.; Zhu, H. L.; Pang, G. H.; Zheng, W. J.; Wong, Y. S.; Chen, T. F. Cancer-Targeted Monodisperse Mesoporous Silica Nanoparticles as Carrier of Ruthenium Polypyridyl Complexes to Enhance Theranostic Effects. *Adv. Funct. Mater.* **2014**, *24*, 2754−2763.
(46) Huang, Y. Y.; He, L. Z.; Liu, W.; Fan, C. D.; Zheng, W. J.; Wong, Y. S.; Chen, T. F. Selective Cellular Uptake and Induction of Apoptosis of Cancer-Targeted Selenium Nanoparticles. *Biomaterials* **2013**, *34*, 7106−7116.
(47) Liu, T.; Lai, L. H.; Song, Z. H.; Chen, T. F. A Sequentially Triggered Nanosystem for Precise Drug Delivery and Simultaneous Inhibition of Cancer Growth, Migration, and Invasion. *Adv. Funct. Mater.* **2016**, *26*, 7775−7790.
(48) Li, S. H.; Guo, Z. X.; Xiong, J.; Lei, Y.; Li, Y. X.; Tang, J.; Liu, J. B.; Ye, J. L. Corrosion Behavior of HVOF Sprayed Hard Face Coatings in Alkaline-Sulfide Solution. *Appl. Surf. Sci.* **2017**, *416*, 69−77.
(49) He, L. Z.; Chen, T. F.; You, Y. Y.; Hu, H.; Zheng, W. J.; Kwong, W. L.; Zou, T. T.; Che, C. M. A Cancer-Targeted Nanosystem for Delivery of Gold(III) Complexes: Enhanced Selectivity and Apoptosis-Inducing Efficacy of A Gold(III) Porphyrin Complex. *Angew. Chem., Int. Ed.* **2014**, *53*, 12532−12536.
(50) Huang, Y. Y.; He, L. Z.; Song, Z. H.; Chan, L.; He, J. T.; Huang, W.; Zhou, B. W.; Chen, T. F. Phycocyanin-Based Nanocarrier as A New Nanoplatform for Efficient Overcoming of Cancer Drug Resistance. *J. Mater. Chem. B* **2017**, *5*, 3300−3314.
(51) You, Y. Y.; He, L. Z.; Ma, B.; Chen, T. F. High-Drug-Loading Mesoporous Silica Nanorods with Reduced Toxicity for Precise Cancer Therapy against Nasopharyngeal Carcinoma. *Adv. Funct. Mater.* **2017**, *27*, 1703313.
(52) Liu, Z.; Chan, L.; Chen, L. Y.; Bai, Y.; Chen, T. F. Facile Fabrication of Near-Infrared-Responsive and Chitosan-Functionalized Cu_2Se Nanoparticles for Cancer Photothermal Therapy. *Chem. - Asian J.* **2016**, *11*, 3032−3039.
(53) Ovechkin, A. S.; Kartsova, L. A. Methods for the Detection and Determination of Singlet Oxygen. *J. Anal. Chem.* **2015**, *70*, 1−4.
(54) Song, Z. H.; Liu, T.; Chen, T. F. Overcoming Blood-Brain Barrier by HER2-Targeted Nanosystem to Suppress Glioblastoma Cell Migration, Invasion and Tumor Growth. *J. Mater. Chem. B* **2018**, *6*, 568−579.

DOI: 10.1021/acsnano.8b06483
ACS Nano 2018, 12, 12401−12415

(55) Chan, L.; He, L. Z.; Zhou, B. W.; Guan, S. H.; Bo, M. J.; Yang, Y. H.; Liu, Y.; Liu, X.; Zhang, Y. Y.; Xie, Q.; Chen, T. F. Cancer-Targeted Selenium Nanoparticles Sensitize Cancer Cells to Continuous Radiation to Achieve Synergetic Chemo-Radiotherapy. *Chem. - Asian J.* **2017**, *12*, 3053−3060.
(56) He, L. Z.; Lai, H. Q.; Chen, T. F. Dual-Function Nanosystem for Synergetic Cancer Chemo-/Radiotherapy through ROS-Mediated Signaling Pathways. *Biomaterials* **2015**, *51*, 30−42.
(57) Huang, Y. Y.; Huang, W.; Chan, L.; Zhou, B. W.; Chen, T. F. A Multifunctional DNA Origami as Carrier of Metal Complexes to Achieve Enhanced Tumoral Delivery and Nullified Systemic Toxicity. *Biomaterials* **2016**, *103*, 183−196.
(58) Ma, B.; He, L. Z.; You, Y. Y.; Mo, J. B.; Chen, T. F. Controlled Synthesis and Size Effects of Multifunctional Mesoporous Silica Nanosystem for Precise Cancer Therapy. *Drug Delivery* **2018**, *25*, 293−306.
(59) He, L. Z.; Huang, Y. Y.; Chang, Y. Z.; You, Y. Y.; Hu, H.; Leong, K. W.; Chen, T. F. A Highly Selective Dual-Therapeutic Nanosystem for Simultaneous Anticancer and Antiangiogenesis Therapy. *J. Mater. Chem. B* **2017**, *5*, 8228−8237.
(60) Huang, W.; Huang, Y. Y.; You, Y. Y.; Nie, T. Q.; Chen, T. F. High-Yield Synthesis of Multifunctional Tellurium Nanorods to Achieve Simultaneous Chemo-Photothermal Combination Cancer Therapy. *Adv. Funct. Mater.* **2017**, *27*, 1701388.
(61) Shi, C. Z.; Liu, D. X.; Xiao, Z. Y.; Zhang, D.; Liu, G. F.; Liu, G. S.; Chen, H. W.; Luo, L. P. Monitoring Tumor Response to Antivascular Therapy Using Non-Contrast Intravoxel Incoherent Motion Diffusion-Weighted MRI. *Cancer Res.* **2017**, *77*, 3491−3501.
(62) Liu, T.; Zeng, L. L.; Jiang, W. T.; Fu, Y. T.; Zheng, W. J.; Chen, T. F. Rational Design of Cancer-Targeted Selenium Nanoparticles to Antagonize Multidrug Resistance in Cancer Cells. *Nanomedicine* **2015**, *11*, 947−958.

DOI: 10.1021/acsnano.8b06483
ACS Nano 2018, 12, 12401−12415

Supporting Information

Sequentially Triggered Delivery System of Black Phosphorus Quantum Dots with Surface Charge Switching Ability for Precise Tumor Radiosensitization

Leung Chan[1], Pan Gao[1], Wenhua Zhou[2], Chaoming Mei[1], Yanyu Huang[1], Xue-Feng Yu[2,*], Paul K. Chu[3], Tianfeng Chen[1,*]

[1] Department of Chemistry, Jinan University, Guangzhou, 510632, P. R. China

[2] Center for Biomedical Materials and Interfaces, Shenzhen Institutes of Advanced Technology, Chinese Academy of Sciences, Shenzhen 518055, P. R. China

[3] Department of Physics and Department of Materials Science and Engineering, City University of Hong Kong, Tat Chee Avenue, Kowloon, Hong Kong, China

*To whom correspondence should be addressed; Tel: +86 20-85225962.

*_Corresponding authors_: Tel: +86 20-85225962.

E-mails: tchentf@jnu.edu.cn (T. Chen); xf.yu@siat.ac.cn (X. F. Yu).

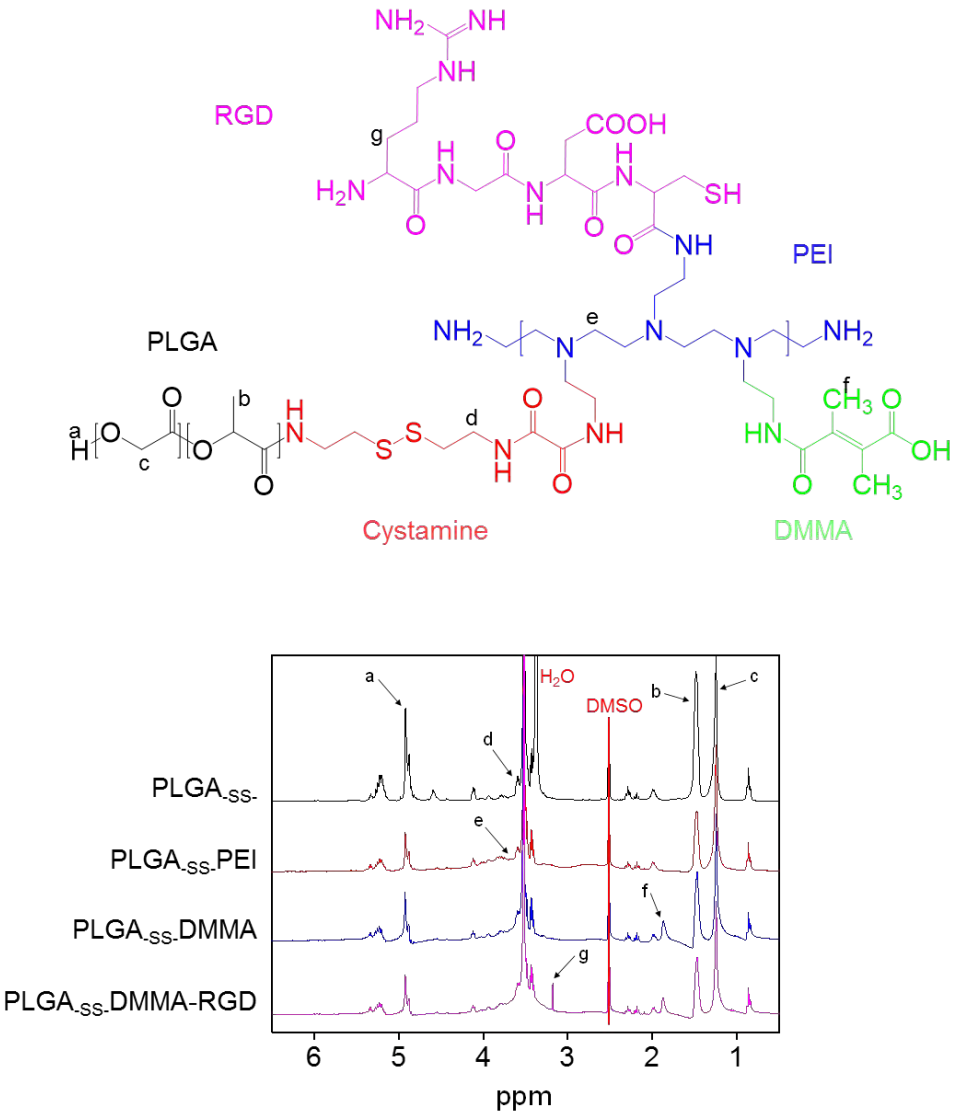

Figure S1. ^{1}H-NMR of PLGA$_{-SS-}$DMMA.

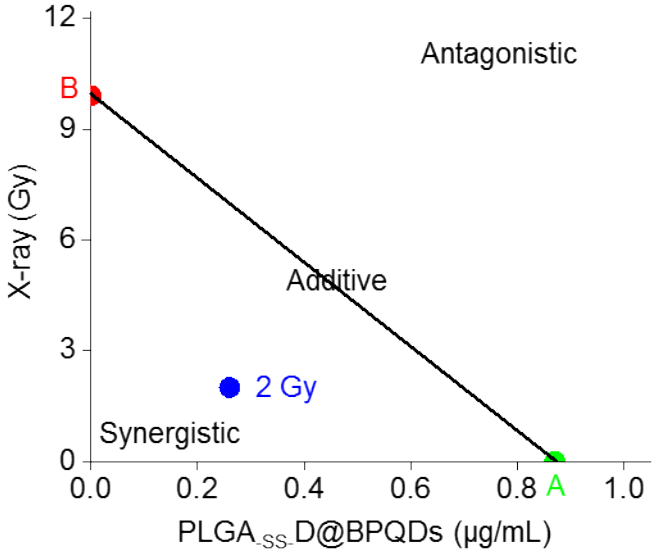

Figure S2. Isobologram analysis of the synergistic antiproliferative effect of the combined application of X-ray and PLGA-SS-D@BPQDs on A375 cells. The data points in the isobologram correspond to the growth inhibition ratio at 50% in the combined treatment.

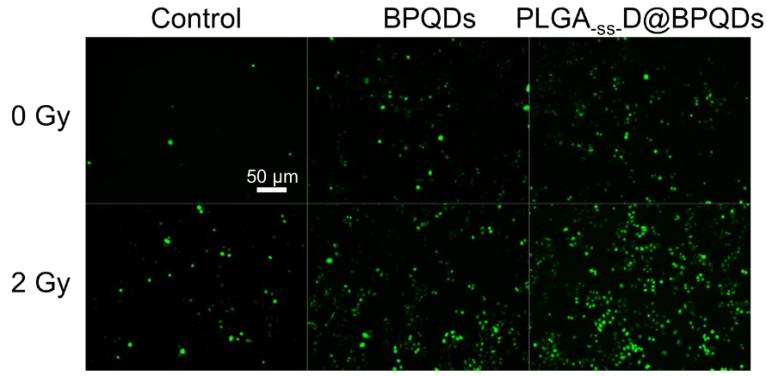

Figure S3. ROS fluorescence images of A375 cells treated with BPQDs, PLGA$_{-SS-}$D@BPQDs, BPQDs + X-ray and PLGA$_{-SS-}$D@BPQD + X-ray at 30 min.